nature materials

Article

https://doi.org/10.1038/s41563-025-02397-2

Mechano-induced patterned domain formation by monocytes

Received: 20 September 2023

Accepted: 7 October 2025

Published online: 05 November 2025

Check for updates

Wenxuan Du D^{1,2,9}, Jingyi Zhu^{2,3,9}, Yufei Wu^{2,4,9}, Hongyi Liu D⁵, Ashley L. Kiemen 12,5, Zegi Wan^{2,6}, Eban Andrew Hanna 12, Hui Zhang^{5,7}, Sean X. Sun © 2,4,7 🖂 & Denis Wirtz © 1,2,5,7,8

Matrix stiffness and the corresponding mechanosignalling play indispensable roles in cellular phenotypes and functions. How tissue stiffness influences the behaviour of monocytes, a major circulating leukocyte of the innate system, and how it may promote the emergence of collective cell behaviour is less understood. Here we show that human primary monocytes, uniquely among key immune cells, undergo a dynamic local phase separation to form highly regular, reversible, multicellular, multilayered domains on soft collagen-coated hydrogels of physiological stiffnesses. Local activation of the β2 integrin–ICAM-1 complex initiates intercellular adhesion, while global soluble inhibitory factors maintain the steady-state domain pattern over days. While inhibiting their phagocytic capability, domain formation promotes the survival of monocytes. A computational model incorporating the Cahn-Hilliard equation of phase separation with the Turing mechanism of local activation and global inhibition suggests that cell seeding density and chemotactic and random cell migration contribute to domain pattern formation, which is experimentally validated. This work reveals that cells can generate complex phases by exploiting their mechanosensing abilities and combined short-range interactions and long-range signals to enhance their survival.

Human tissues span a wide range of stiffnesses¹, ranging from 11 Pa (intestinal mucus) to 20 GPa (cortical bone)², which also vary with ageing and disease³⁻¹⁰. Cells have evolved complex molecular mechanisms to sense and respond to these different environmental mechanical cues to differentiate, signal and migrate. How immune cells respond to mechanical cues has received notably less attention. In particular how monocytes, which are pivotal components of the innate immune response, respond to microenvironments of different stiffness is not well understood¹¹. Microenvironmental signals can differentiate monocytes into macrophages and dendritic cells, which enables them to orchestrate innate and adaptative immune responses^{12,13}. Upon infection, inflammation or tumorigenesis, classical CD14⁺CD16⁻ monocytes that mature in the bone marrow and emigrate to the peripheral blood traffic between blood vessels and soft tissues¹⁴, making them more likely to encounter microenvironments of different stiffness.

Immune cell aggregation is a physiologically relevant process that plays a vital role in pathogen clearance and cancer metastasis for B cells^{15,16}, neutrophils^{17,18}, dendritic cells¹⁹ and monocytes/macrophages²⁰. Imaging of precancer lesions and tumours has also revealed spatially heterogeneous immune cell hot-spots-dense aggregates

¹Department of Chemical and Biomolecular Engineering, Johns Hopkins University, Baltimore, MD, USA. ²Institute for NanoBioTechnology, Johns Hopkins University, Baltimore, MD, USA. 3Department of Biomedical Engineering, Johns Hopkins University, Baltimore, MD, USA. 4Department of Mechanical Engineering, Johns Hopkins University, Baltimore, MD, USA. 5Department of Pathology, Johns Hopkins University School of Medicine, Baltimore, MD, USA. ⁶Department of Biochemistry and Molecular Biology, Johns Hopkins University, Baltimore, MD, USA. ⁷Johns Hopkins Physical Sciences—Oncology Center, Johns Hopkins University, Baltimore, MD, USA. 8Department of Oncology, Johns Hopkins University School of Medicine, Baltimore, MD, USA. 9These authors contributed equally: Wenxuan Du, Jingyi Zhu, Yufei Wu. 🖂 e-mail: ssun@jhu.edu; wirtz@jhu.edu

of immune cells^{21–24}. Cells connect with neighbouring cells and their milieu via adhesion molecules, including cadherins, selectins, integrins, immunoglobulin (lg)-like adhesion molecules and mucins²⁵. Integrins are highly expressed on the surface of monocytes, which are essential for the tethering and rolling process of extravasation and a mediator of cell–matrix adhesion via focal adhesion complexes^{26–28}. Whether and how matrix mechanical properties modulate immune cell aggregation is unclear.

Immune cell aggregates are reminiscent of dynamic phases observed in active matter systems²⁹. In particular, flocking transitions during collective movement of fish and birds also produce high-density aggregates^{30,31}. Recent theoretical work has revealed the rich phase behaviour of self-propelled particles and their underlying microscopic interactions³²⁻³⁵. Different from flocking, which is governed by local short-range interactions between self-driven particles, cells feature both short-range interactions and produce long-range signals via secreted molecules and therefore could generate complex collective behaviour distinct from conventional active matter. In particular, cells can respond to differences in matrix stiffness, secrete factors, proliferate and undergo chemotaxis. Moreover, cell movement is distinct from propelled particles and is described by persistent random walks^{36,37}. These distinct aspects led us to hypothesize that immune cells could collectively produce new dynamic phases and behaviours.

In this study, we find that matrices of low stiffness can trigger pattern domain formation by monocytes via overexpression of $\beta 2$ integrin and ICAM-1 on their surface to promote cell survival. We propose a phenomenological model based on the Turing mechanism and the Cahn–Hilliard equation for phase transitions 38,39 , which incorporates a $\beta 2$ integrin–ICAM-1 complex as a local activator and soluble factors secreted by aggregated monocytes as global inhibitors, which promotes pattern formation on soft matrix. The effects of cell seeding density and cell migration on patterns are predicted by computational simulations and validated in corresponding experiments.

Soft matrix induces monocyte multicellular domain formation

This paper explores the emergence of collective phenomena resulting from monocytes exposed to substrates of different stiffnesses. But we first place our work in a biological context. Localized high-density regions of leucocytes can be observed in both non-diseased tissues and precursor lesions in human pancreas (Supplementary Fig. 1a). This indicates that leucocytes may collectively aggregate upon encountering areas of stiffness in a physiological matrix after leaving the circulation. The function and mechanism of such domains remain unclear. To narrow down the composition of such hot-spots, we stained pancreatic tissue with pan-monocyte/macrophage marker CD68 and identified high-density regions of monocytes/macrophages (Supplementary Fig. 1b).

To investigate the conditions necessary for monocytes to form such aggregates in vitro and to assess the potential role of matrix stiffness, we placed freshly isolated human classical CD14 $^+$ CD16 $^-$ monocytes on polyacrylamide gel substrates of physiological stiffnesses, 0.5 kPa and 100 kPa, and on standard cell culture plastic substrates (~5 GPa). These substrates were chosen to mimic the range of tissue stiffness encountered by monocytes during disease progression, such as the transition from the relatively soft microenvironment of the normal human breast to the comparatively stiffer microenvironment of a breast tumour 40. All substrates in this work were coated with a saturating amount of collagen I—the main constituent of the extracellular matrix in stromal spaces—to keep the biochemical ligand presentation to the cells constant.

Following seeding as a monolayer on a 0.5-kPa substrate (healthy tissue), monocytes remained mostly featureless for an 'incubation' time of 1–2 h. This incubation time, during which monocytes remained a monolayer, was remarkably consistent across donors and across

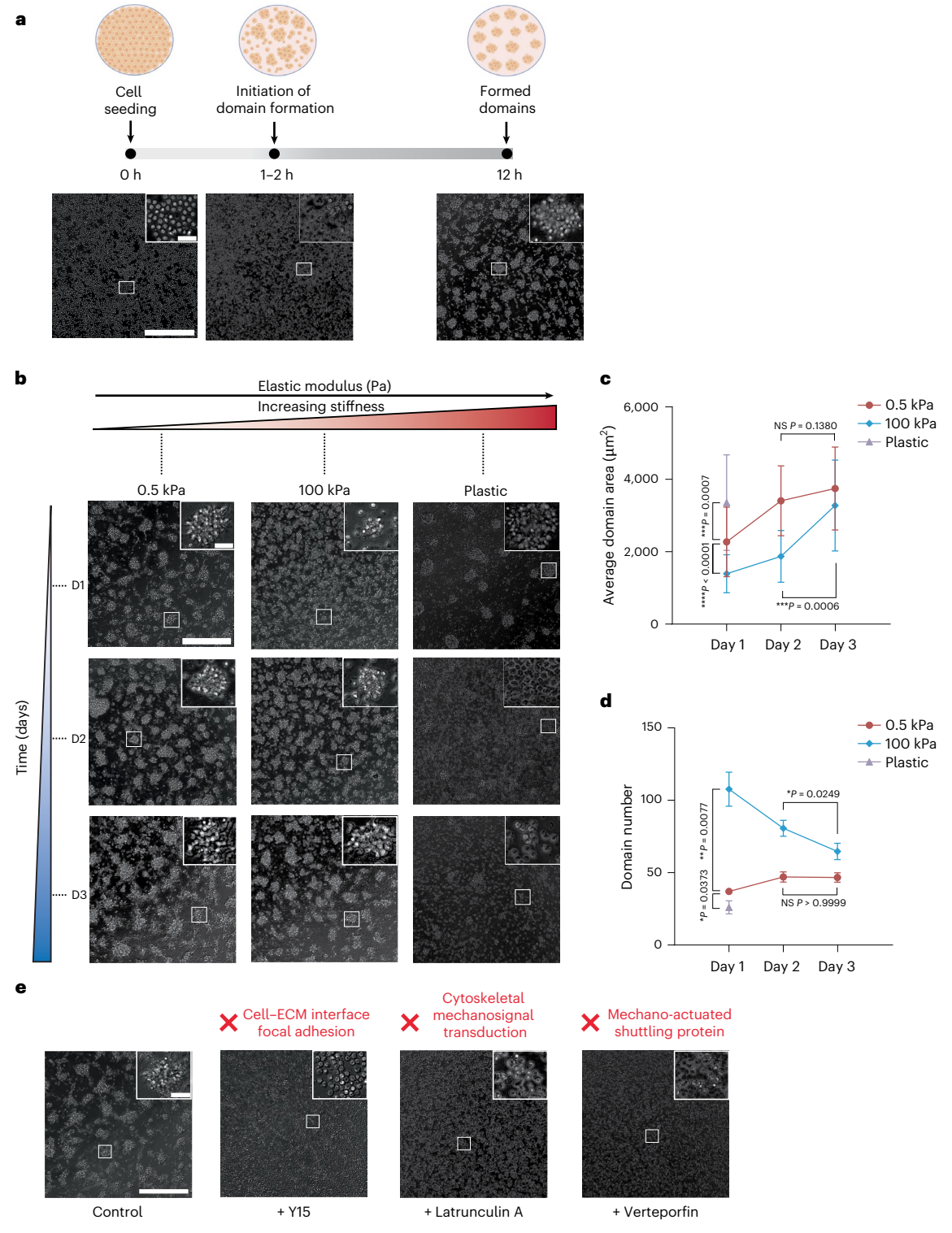
different wells for a given donor (Supplementary Fig. 1c,d). Then a rapid phase separation occurred, and multicellular aggregates formed (Supplementary Video 1). During the first few hours post-transition, the borders of these aggregates were diffuse. After ~12 h, these aggregates annealed and formed well-defined multilavered aggregates that were spatially patterned, referred to below as 'domains' (Fig. 1a). Domain formation of monocytes placed on a 100-kPa substrate (diseased tissue) was also observed but experienced a substantial delay that resulted in the development of irregular and smaller domains on day 1 (Fig. 1b,c). On plastic culture dishes, monocytes formed highly transient aggregates, with an average size that was larger than that of the aggregates formed on the 0.5-kPa and 100-kPa substrates on day 1 (Fig. 1c). These aggregates collapsed after day 2 (Fig. 1b). On the 0.5-kPa substrate, monocytes quickly developed domains on day 1 and, unlike for the 100-kPa substrate, this pattern remained relatively consistent from day 2 to day 3, for which domain area and number plateaued (Fig. 1c,d and Supplementary Video 2). Note that long-term culture of monocytes may lead to changes in phenotype, including differentiation, which limits our experimental window. Here we refer to the domain pattern on the 0.5-kPa substrate on day 3 as the experimental 'steady state'. Therefore, for the mechanistic investigations below, we will mostly use the 0.5-kPa substrate and its associated fast kinetics of domain formation.

The CD45⁺ immune hot-spots observed in pancreatic tissue (Supplementary Fig. 1a) may be a mixture of monocytes, macrophages and lymphocytes. We thus asked if our observed stiffness-mediated patterned domains of monocytes were produced by other immune cells. We placed either primary human monocyte-derived (M0 naïve) macrophages, B cells, natural killer (NK) cells or T cells on the 0.5-kPa substrate and assessed potential phase separation. None of these lymphocytes could initiate ordered domain formation when exposed to mechanical cues within the first 24 h, which suggests the unique ability of monocytes to form patterned aggregates via mechanosensing. Instantly after seeding, macrophages aggregated but formed continuous cell clusters instead of spatially distinct patterned domains. The majority of these macrophage aggregates collapsed and disappeared on day 2 and individual cells with mesenchymal morphology were observed on day 3 (Extended Data Fig. 1a). T cells remained as a monolayer for 3 days, while NK cells only formed small, sparsely distributed, diffuse clusters. For B cells, which are known to aggregate following stimulation¹⁵, we observed patterned domain formation after 48 h, but these domains subsequently merged, prompting a macroscopic phase separation. These large aggregates even partially detached from their substrates (Extended Data Fig. 1a). Finally, after long-term activation with IL-2 cytokine before seeding, both B and NK cells aggregated instantly to subsequently undergo macroscopic phase separation (Extended Data Fig. 1b). T cells activated with IL-2 and CD3/ CD28 Dynabeads mostly remained as a monolayer, coexisting with a few small clusters (Extended Data Fig. 1b). In sum, only freshly isolated monocytes formed long-lived, highly patterned aggregates following exposure to a soft substrate.

To further support the hypothesis that monocyte domain formation was mechano-induced, we targeted mechanosensing and transduction comprehensively 41,42 . Upon inhibition of the major mechanosensing protein focal adhesion kinase (FAK) $^{43-45}$, monocytes did not exhibit domain formation (Supplementary Video 3). The same was observed when monocytes were treated with the actin destabilizer latrunculin $\rm A^{41}$ and with the inhibitor of YAP/TAZ-based mechanotransduction verteporfin $^{41,46-48}$ (Fig. 1e). These data further support that mechanosensing plays an indispensable role in the process of domain formation by monocytes.

Phase separation promotes survival and inhibits phagocytosis

Next, we investigated possible functional outcomes of monocyte domain formation. Monocytes seeded on the 0.5-kPa substrate showed



 $\label{eq:continuous} \textbf{Fig. 1} | \textbf{Mechano-induced domain formation of human primary monocytes.} \\ \textbf{a}, \textbf{Human primary classical (CD14+CD16-) monocytes formed compact} \\ \textbf{multicellular domains when placed on a 0.5-kPa collagen I-coated substrate.} \\ \textbf{Monocytes spontaneously form predomain spots around 1-2 h after initial} \\ \textbf{seeding. After 12 h of incubation, these spots progress to highly patterned} \\ \textbf{domains (Supplementary Video 1). b, Representative images of monocytic domain formation on 0.5-kPa, 100-kPa and plastic collagen I-coated substrates obtained on day 1, day 2 and day 3. c, Average area of domains formed by monocytes on substrates of different stiffnesses at different time points. Monocytic domains collapsed on collagen-coated plastic substrates and were therefore not characterized on day 2 and day 3. A slightly enlarged (not significant) domain area was observed on the 0.5-kPa substrate from day 2 to day 3, which was potentially caused by 'flattening' of the multilayered domain structure.$ **d**, Average number of

domains formed by monocytes on substrates of different stiffnesses at different time points. Domains collapsed on collagen-coated plastic substrates and were therefore not characterized on day 2 and day 3. **e**, Inhibition of focal adhesion kinase using 20 μ M Y15, destabilization of the F-actin network using 200 nM latrunculin A and inhibition of YAP/TAZ using 1 μ M verteporfin all abrogated monocyte domain formation on day 1. ECM, extracellular matrix. Representative images in **a,b,e** were obtained with a phase-contrast microscope under a 20× objective. Scale bars, 300 μ m and 30 μ m (insets). Domain characteristics data in **c,d** are presented as mean \pm s.d.; N=3 donors, n=3 independent biological samples for **c,d**. A two-tailed non-parametric Mann–Whitney test was used for statistical analysis (****P \leq 0.001, ***P \leq 0.001) for **c**. A two-tailed unpaired t-test with Welch's correction was used for statistical analysis (***P \leq 0.01, *P \leq 0.05) for **d**. NS, not significant (*P*> 0.05). Cartoon in **a** created with BioRender.com.

significantly higher viability than monocytes seeded on plastic and glass substrates within 72 h, for which collapsed domains and cellular apoptosis were clearly observed (Extended Data Fig. 2a). A quantitative cell-viability assay showed a dramatic decrease in signal from monocytes on plastic and glass substrates compared with monocytes on the 0.5-kPa substrate. This result indicates an underlying functional con $nection\,between\,the\,ability\,of\,monocytes\,to\,form\,and\,maintain\,domains$ and their viability (Extended Data Fig. 2b). Monocytes were also harvested from different substrates and analysed using flow cytometry. While debris remained at a relatively low value of 10.7% for monocytes harvested from the 0.5-kPa substrate, an elevated proportion of debris were observed on stiffer substrates, namely, 25.1% for plastic and 77.1% for glass (Extended Data Fig. 2c). Finally, more monocytes positive for propidium iodide were observed through immunofluorescence imaging and flow cytometry, which worked as extra validations of reduced cell viability on non-physiological substrates (Extended Data Fig. 2c). In contrast to freshly isolated monocytes, the majority of activated lymphocytes died after 3 days in culture (Extended Data Fig. 1). These results suggest that monocytes aggregate to survive.

To study whether domain formation had any impact on the phagocytic ability of monocytes, we evaluated the number of internalized carboxylate-modified polystyrene fluorescent beads. We distinguished monocytes located within the domains as 'insiders' and those outside the domains as 'outsiders' (Extended Data Fig. 2d). On the 0.5-kPa substrate, insiders and outsiders exhibited similar levels of bead phagocytosis. Likewise, on the plastic substrate, there was no significant difference in phagocytosis ability between insiders and outsiders (Extended Data Fig. 2e). However, 'insiders' on the 0.5-kPa substrate displayed a small but statistically significant lower phagocytic activity than those on plastic substrate, which suggests a negative correlation between monocyte viability and phagocytosis.

β2 integrin and ICAM-1 mediate cell aggregation

Previous work on the monocytic cell line U937 reported the involvement of LFA-1/VLA-4 in the intercellular adhesion of these cells on tissue culture plastic^{49,50}. Here, we hypothesized that integrins mediated domain formation of monocytes. We compared the expression of integrin subunits for monocytes collected from collagen I-coated 0.5-kPa substrate at different time points. Among tested integrins, we found that integrin $\alpha 4$, αM and $\beta 2$ exhibited increased expression by day 3, for which we observed well-defined stable domain patterns, compared with day 1 (onset of domain formation). This suggested a potential role of $\alpha 4$, αM and $\beta 2$ in inducing domain formation (Fig. 2a). To validate these findings, we treated monocytes immediately after seeding with inhibitory antibodies targeting these three upregulated integrins. Only the anti-β2 integrin antibody completely abrogated domain formation (Fig. 2b). Moreover, the application of this antibody after domains had formed eliminated these domains (Fig. 2c and Supplementary Video 4). These results suggest that β2 integrin is a main mediator of domain formation and show that domain formation is reversible.

To further establish cause and effect, we examined the effect of stimulatory antibodies specific to $\beta 2$ integrin (clones m24 and LFA-1/2) and found that these antibodies accelerated the initiation of monocyte domain formation (Supplementary Video 5), resulting in highly organized patterns after domain initialization with increased domain area and number (Fig. 2d–f). In sum, $\beta 2$ integrin is directly involved in the domain formation of monocytes on soft matrix.

Since domain formation and progression differed for the tested substrate stiffnesses, we hypothesized that the level of expression of $\beta 2$ on monocytes placed on different substrates would vary accordingly. Reverse transcription quantitative polymerase chain reaction (RT-qPCR) analysis was performed on samples collected on days 1 and 3, representing the initialization stage and stabilization/collapse stage of domains on the 0.5-kPa, 100-kPa and plastic substrates. Despite a slight downregulation of $\beta 2$ on day 1, we observed elevated mRNA

expressions of $\beta 2$ on the 0.5-kPa and 100-kPa substrates, but not on plastic substrate (on day 3), which correlated well with the domain pattern maintenance shown in Fig. 1c (Extended Data Fig. 3a). These results were validated via flow cytometry: the surface expression of $\beta 2$ was already high on day 0 for isolated monocytes, with a slight decrease on day 1 for all three substrates and upregulation on day 3 for the 0.5-kPa and 100-kPa substrates (Extended Data Fig. 3a).

To identify the ligand for β2 integrin that drove monocyte aggregation, we chose six potential cell-surface targets, including CD14 (ref. 51), CD23 (ref. 52), ICAM-1, ICAM-2, ICAM-3 and ICAM-4 (refs. 26,53), and tested their time-dependent mRNA expression on the 0.5-kPa substrate. ICAM-1 expression increased both on day 1 and day 3, with a higher fold change compared with β2 integrin (Extended Data Fig. 3b). This identified ICAM-1 as a potential inducer of domain initialization. Via flow cytometry, we observed significant upregulation of ICAM-1 surface expression on monocytes seeded on the 0.5-kPa and 100-kPa substrates (Extended Data Fig. 3c). Surprisingly, even monocytes seeded on plastic substrate upregulated ICAM-1 expression in spite of their inability to maintain patterned domains long term. Functionally blocking ICAM-1 successfully prevented the onset of domain formation (Extended Data Fig. 3d), increased cellular apoptosis and decreased PrestoBlue signal (Extended Data Fig. 4a,b). Taken together, the upregulated β2 integrin-ICAM-1 molecular pair is indispensable for driving intercellular monocyte adhesion and mediating domain formation.

Monocytes secrete global inhibitors

Importantly, global phase separation of the monocyte/buffer system into a large monocyte-rich domain and a monocyte-poor domain that resembles full coarsening did not occur, even for long observation times (3 days). Because these steady-state domains resulted from multiple domains that coalesced, we proposed the existence of monocyte-secreted inhibitory soluble factors that partially inhibited intercellular adhesion in the system, referred to here as 'global inhibition', which stabilized the microdomain pattern. To ascertain this hypothesis, the medium that potentially contained inhibitory factors was aspirated and fresh medium was placed onto the culture on day 1 after domain initialization (Fig. 3a). Upon removal of the 'global inhibitors', domain coalescence was observed, whereby adjacent domains migrated and merged (Supplementary Video 6). Within 24 h, quasi-macrophase separation was achieved (Fig. 3b). In addition, conditioned medium obtained from monocyte domains formed on the 0.5-kPa substrate was harvested, serially diluted and applied to a monolayer of freshly seeded monocytes (Extended Data Fig. 5a). Monocytes treated with 2× diluted 0.5-kPa conditioned medium abolished domain formation (Extended Data Fig. 5b), presumably due to the high concentration of inhibitory soluble factors secreted by monocytes. Monocytes cultured in 8× diluted conditioned medium showed delayed domain formation and showed significantly smaller domain sizes and decreased migration compared with control monocytes on day 1 after domain initialization (Extended Data Fig. 5b,c).

To further investigate whether inhibitory factors were produced by the aggregated 'domained' monocytes to stabilize the domain pattern, we harvested conditioned medium from monocytes seeded on different substrates (Fig. 3c). Conditioned medium harvested from glass substrate where monocytes remained as a monolayer failed to delay the domain initialization due to lack of inhibitory factors. In contrast, conditioned media harvested from cells on the 0.5-kPa and 100-kPa substrates both decreased domain areas and increased domain numbers, indicating delayed domain initialization (Fig. 3d,e). Conditioned medium from the 0.5-kPa substrate inhibited domain formation more significantly than conditioned medium from the 100-kPa substrate with smaller domain area on day 1 (Fig. 3d) and slower kinetics of domain initialization (Supplementary Video 7). This is potentially due to a higher concentration of inhibitory factors, resulting from the faster kinetics of domain formation on the 0.5-kPa substrate (Fig. 1b).

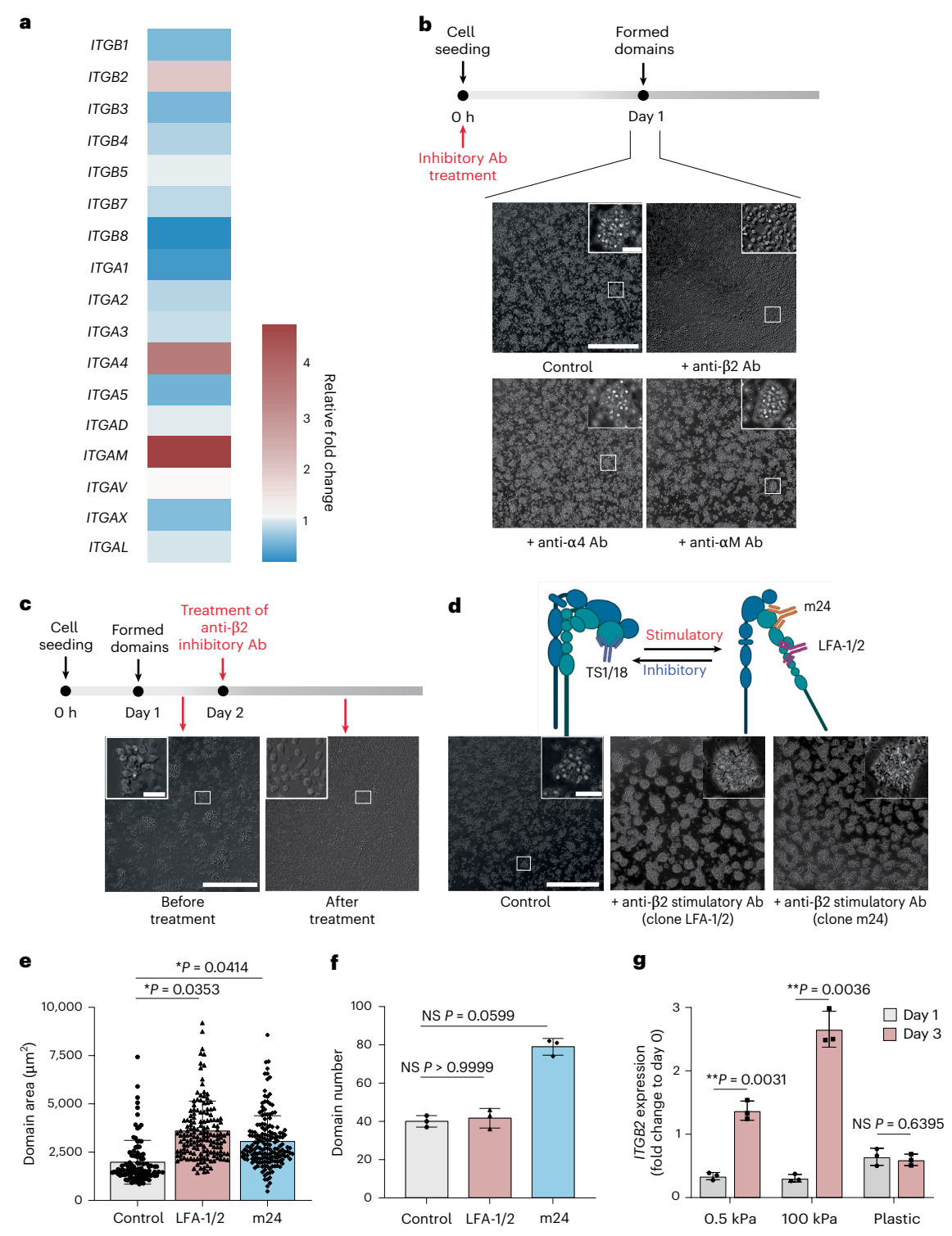


Fig. 2 | **β2** integrin mediates stiffness-dependent monocyte domain formation. a, RT-qPCR analysis of integrin mRNA expression profile from cells collected on day 1 and day 3 from 0.5-kPa substrate. Relative fold changes of different integrins were measured relative to day 1. **b**, Representative images of domain formation when monocytes were treated during seeding with inhibitory antibodies (Ab) against integrins β2, α 4 and α M. **c**, Representative images of reversible domain collapse observed on day 2 after formation when cells were treated with inhibitory β2 antibody. **d**, Cartoon showing different binding subunits of inhibitory (clone TS1/18) and stimulatory β2 antibodies (clone m24 and LFA-1/2). Representative images taken at 6 h after seeding showed induced onset of domain formation when monocytes were treated with a stimulatory β2 antibody. **e**, **f**, Characterization of domain area (**e**) and domain number (**f**) at 6 h when monocytes were treated with stimulatory β2 antibodies. **g**, RT-qPCR

analysis of ITGB2 expression in monocytes on collagen I-coated 0.5-kPa, 100-kPa and plastic substrates. The expression of ITGB2 correlated well with the domain development over a 3-day period on different substrates. Relative fold changes in expression of different integrins were measured relative to day 0. Representative images in $\mathbf{b}-\mathbf{d}$ were obtained with a phase-contrast microscope under a $20\times$ objective. Scale bars, $300~\mu\mathrm{m}$ and $30~\mu\mathrm{m}$ (insets). Data in $\mathbf{e}-\mathbf{g}$ are presented as mean \pm s.d.; N=3 donors, n=3 independent biological samples for $\mathbf{a},\mathbf{g}; n=3$ independent biological samples in \mathbf{e},\mathbf{f} ; all individual domains were measured from three independent biological samples and plotted together in \mathbf{e} . A Kruskal–Wallis test with Dunn's multiple-comparisons test was used for statistical analysis (* $P \le 0.05$) for \mathbf{e},\mathbf{f} . A two-tailed unpaired t-test with Welch's correction was used for statistical analysis (* $P \le 0.05$). Cartoon in \mathbf{d} created with BioRender.com.

To identify these inhibitory factors, we separated the conditioned medium harvested from the 0.5-kPa substrate into large- and small-molecule portions via ultracentrifugation. While the unfiltered and the protein portion of the conditioned medium significantly hindered domain formation, resulting in smaller domain areas and larger domain numbers, small molecules failed to induce inhibition (Extended Data Fig. 5d,e). This result suggested that secreted proteins from 'domained' monocytes drive the global inhibition. Next, a proteomic assay was carried out to identify candidate proteins (Extended Data Fig. 6a). Enrichment analysis revealed that the upregulated proteins were mainly enriched in TNF signalling via NFκB, Myc targets V1, mTORC1 signalling and hypoxia pathways (Extended Data Fig. 6b). Among upregulated proteins, we intersected the top 20 proteins with the highest fold change and the top 20 proteins with the highest expression level and found candidate proteins to be chitinase-3-like protein 1 (CHI3L1) and interleukin-8 (IL-8) (Extended Data Fig. 6c). Next, we analysed monocytic domain formation with exogenously added purified CHI3L1, IL-8 or a combination of both CHI3L1 and IL-8, This analysis validated CHI3L1 as a global inhibitor for mechano-induced monocyte domain formation (Extended Data Fig. 6d,e).

Computational model predicts domain formation

This spontaneous, reversible, patterned aggregation of monocytes resembles the motility-induced phase separation of active matter 32,54,55 and displays properties of pattern formation described by the Turing mechanism⁵⁶. To further explore this microdomain formation by monocytes, we developed a computational model based on the Cahn-Hilliard approach^{38,39}. This model describes phase separation whereby the two components of a binary fluid (monocytes + surrounding medium) spontaneously separate into domains rich in one of the two components. Diffusible inhibitory factors were introduced to the system following the 'global inhibition' theory that we proposed and validated. Production, diffusion and degradation of these soluble molecules were combined together to shape their distribution. Considering the consistent initiation time of monocyte domain formation (Supplementary Fig. 1c) and the upregulation of the β2–ICAM-1 pair during domain formation and maintenance, we assumed an elevated affinity and expression of cell adhesion molecules as the driving force for phase-separation initialization, which we referred to as 'local activation'. In the experiments, the height of the culture medium is negligible compared to the dish. hence we used a two-dimensional model.

The parameters and variables used for modelling the domain formation process are listed in Supplementary Table 1. Due to the slow proliferation of human primary monocytes (Extended Data Fig. 2b), cell growth was ignored for simplification. We describe the cells in a continuum model using an effective free-energy density functional of the form $F = \int d\mathbf{r} [k_4(c_1\rho^4 + c_2\rho^3 + c_3\rho^2) + \frac{1}{2}[k_3e^{-\alpha c} + \epsilon](\nabla\rho)^2]$. Here, ρ and c are the cell density and concentration of inhibitory molecules, respectively. The first term of this equation is the prototypical bulk free energy of a hard-core particle with short-range attraction, which roughly describes cells with mutual adhesion. The second term

represents the interfacial energy between cells and the surrounding medium, which we hypothesized was negatively influenced by inhibitory molecules, following a declining exponential function, characterized by a decaying coefficient. A small threshold $\epsilon > 0$ is added to the interfacial energy coefficient to ensure interfacial stability. The exponential dependence of the gradient term in the free energy can be understood as chemokine-dependent regulation of cell-cell attraction, which changes the effective 'surface tension' from expression of molecules such as β 2. The regulation of expression in cells is typically cooperative and the concentration dependence often follows a Hill function, modelling the fact that binding can saturate, depending on binding constants. The exponential function models the rapid change component of the Hill function. Given the free-energy function, the 'chemical potential' driving cell motion is $\mu = \frac{\delta F}{\delta \rho}$. Cells also migrate randomly, generating a diffusive behaviour with a flux given by $\mathbf{j} = -D_1 \nabla \mu$. The final equation for cell movement is $\frac{\partial \rho}{\partial t} = -\nabla \cdot \mathbf{j} = D_1 \nabla^2 \mu$. The production and diffusion of inhibitory factors are described by a reaction-diffusion equation. The final governing equations (Supplementary Note 1) for both cells and inhibitory factors are

$$\frac{\partial \rho}{\partial t} = D_1 \nabla^2 [k_4 (4c_1 \rho^3 + 3c_2 \rho^2 + 2c_3 \rho)
+ \alpha k_3 e^{-\alpha c} \nabla c \cdot \nabla \rho - (k_3 e^{-\alpha c} + \epsilon) \nabla^2 \rho]$$
(1)

$$\frac{\partial c}{\partial t} = D_2 \nabla^2 c + k_1 \rho^2 - k_2 c \tag{2}$$

We solved the equations in a square region with side length l. The second term in the inhibitor production models non-linear effects, or the fact that cells tend to autocatalyse production of cytokines⁵⁷. In our model, we assumed no flux at the boundary for both cells and inhibitory molecules. The initial cell density was set with a random small perturbation around a homogeneous state following a uniform distribution. The initial inhibitory molecule concentration was set as zero. To better match the domain area and number characterization results of simulations to experimental conditions, we further defined dimensionless parameters by setting characteristic length L and time T scales (Supplementary Table 1). All the normalized variables and parameters in the equation are defined as: $\widetilde{\rho} = \rho L^2$, $\widetilde{c} = cL^2$, $\widetilde{t} = \frac{t}{T}$, $\widetilde{x} = \frac{x}{L}$, $\widetilde{c_1} = \frac{c_1}{L^4}$, $c_2 = \frac{c_2}{L^2}$, $\widetilde{c_3} = c_3$, $\widetilde{D_1} = \frac{D_1 T}{L^2}$, $\widetilde{\alpha} = \frac{\alpha}{L^2}$, k_4 , k_4 , $k_3 = \frac{k_3}{L^2}$, $\widetilde{D_2} = \frac{D_2 T}{L^2}$, $\widetilde{k_1} = \frac{k_1 T}{L^2}$, $\widetilde{k_2} = k_2 T$. If not specified, the dimensionless parameters were fixed at base values in all simulations (Supplementary Table 1) and the initial cell density was set as $\widetilde{\rho}_i \approx (0.6, 0.7)$. In all simulations, the length and time scales were set as $L = 8 \mu m$ and T = 0.0036 h to match experimental field of view and observation time. The rationale for our parameter selection is provided in Supplementary Note 2. The length scale of the pattern can be obtained by a linear stability analysis, which gives the wavenumber of the dominant

pattern as: $k=\sqrt{-\frac{6c_1\rho_0^2+3c_2\rho_0+c_3}{k_3e^{-ac_0}}}$ (Supplementary Note 3). We can see that an increase in α decreases the length scale of the pattern, and an increase in k_3 increases the length scale, which is validated in the following section.

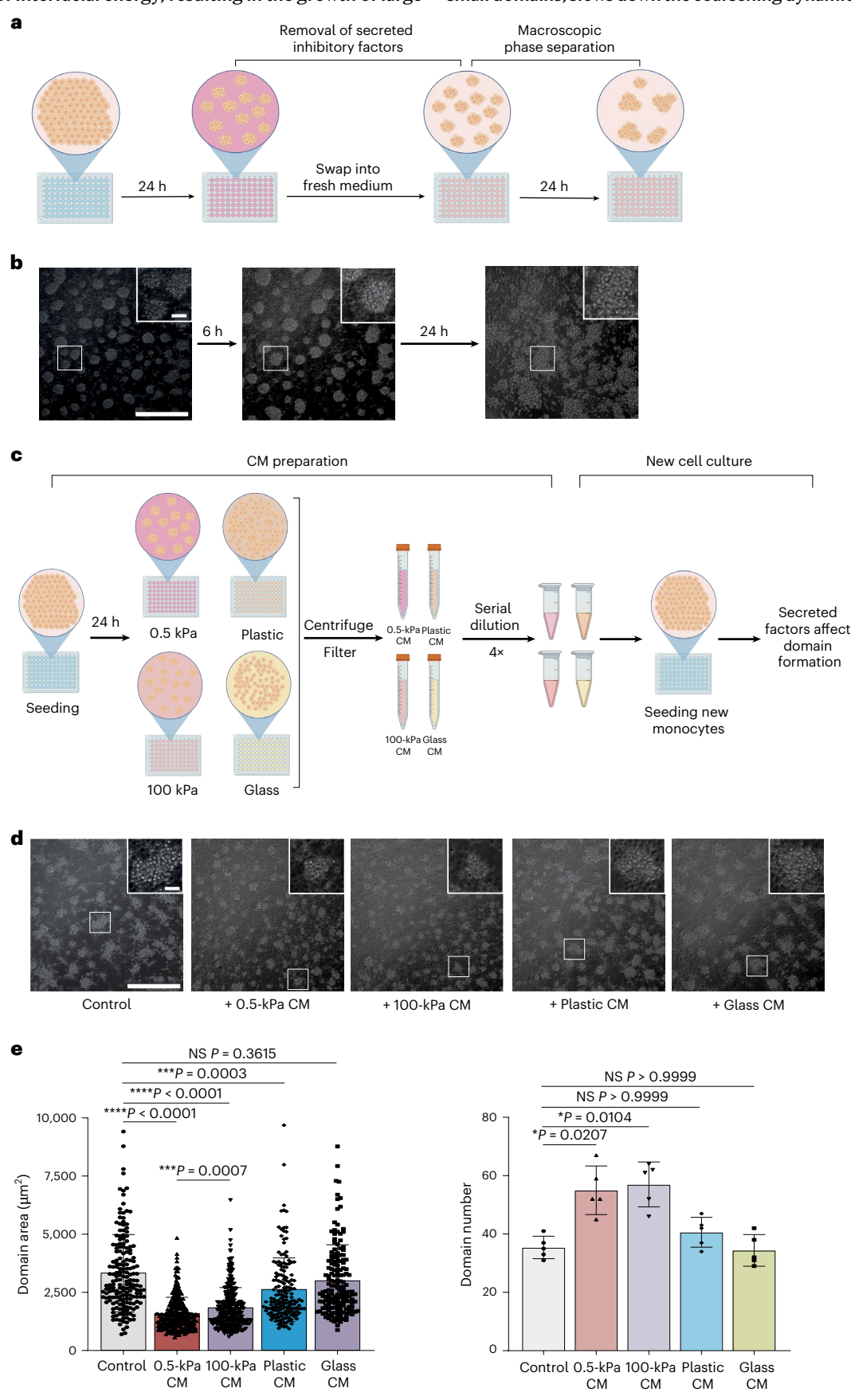
Fig. 3 | Secreted factors from monocytic domains abrogate phase separation.

a, Illustration of how secreted factors are removed. Fresh medium was swapped onto monocyte domains formed on day 1. b, Representative images of monocyte domains at different time points after medium swap. Coalescence of adjacent domains was observed after 6 h and a quasi-macrophase separation was achieved after 24 h. c, Illustration of conditioned medium (CM) collection from different substrates. Domains were formed only on 0.5-kPa and 100-kPa substrates after 24 h. All four conditioned media were diluted 4× to decrease the concentration of inhibitory factors to prevent complete abrogation of domain formation.
d, Representative images of domain formation for freshly seeded monocytes on day 1 under treatment with 0.5-kPa/100-kPa/plastic/glass conditioned medium. e, Characterization of domain area and number showed non-significant

differences between the control and the glass conditioned medium groups, indicating a lack of domain formation inhibition compared with conditioned media harvested from softer substrates. Representative images in ${\bf b}, {\bf d}$ were obtained with a phase-contrast microscope under a $20\times$ objective. Scale bars, $300~\mu{\rm m}$ and $30~\mu{\rm m}$ (insets). Data are presented as mean \pm s.d. with n=5 independent biological samples for ${\bf e}$; all individual domains were measured from five independent biological samples and plotted together in ${\bf e}$. A Kruskal–Wallis test with Dunn's multiple-comparisons test was used for statistical analysis (****P ≤ 0.0001 , ****P ≤ 0.0001) for ${\bf e}$. A two-tailed non-parametric Mann–Whitney test was used for statistical analysis (****P ≤ 0.001) comparing 0.5-kPa and 100-kPa conditioned medium in ${\bf e}$. NS, not significant (P > 0.05). Cartoons in ${\bf a}$, ${\bf c}$ created with BioRender.com.

In a two-component system with mutual attraction and interfacial tension, the system tends to undergo coarsening, evolving toward macroscopic phase-separated domains. This process is driven by the minimization of interfacial energy, resulting in the growth of large

domains at the expense of smaller ones. However, in our system, the interfacial tension is negatively regulated by a diffusible inhibitory factor, as modelled in equation (1). This suppresses the coalescence of small domains, slows down the coarsening dynamics and leads to the



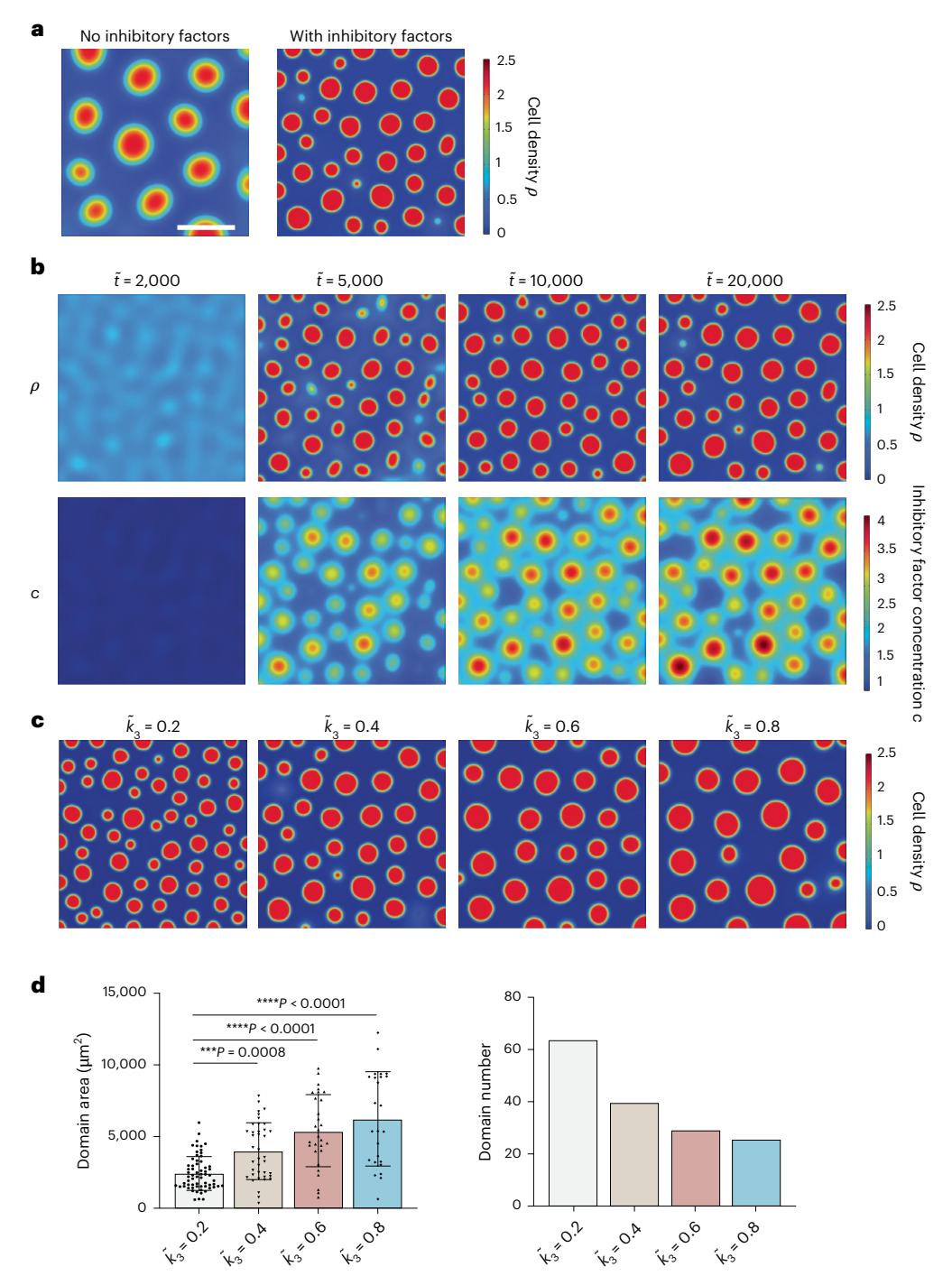


Fig. 4 | **Validation of 'global inhibition, local activation' in the simulation model. a,** Simulation results comparing the steady states with and without the proposed inhibitory factors showed that the lack of inhibitory factors led to fewer, larger domains, characteristic of macrophase separation. **b**, The field heatmap of inhibitory factors at early stages and the steady state correlated well with microdomain pattern. **c**, Insufficient domain formation was observed when 'local activation' was mitigated via setting decreased interfacial coefficient $\widetilde{K_3}$ (all other key parameters fixed at base values). **d**, Characterization of steady domain

area and number showed a monotonic decrease in domain area and increase in domain number when decreasing interfacial coefficient $\widetilde{K_3}$. All simulation results represent steady states. Scale bars, 300 μ m for all simulations. All domain area characterization results are presented as mean \pm s.d.; all individual domains at steady state were measured from each simulation and plotted in \mathbf{d} (n=1 simulation). A Kruskal–Wallis test with Dunn's multiple-comparisons test was used for statistical analysis (**** $P \le 0.0001$, *** $P \le 0.001$) in \mathbf{d} .

stabilization of microdomains—consistent with experimental observations. In the limit where the interfacial energy threshold vanishes ($\epsilon=0$), the coarsening process would be fully arrested, generating stable microdomains. However, in our numerical implementation, setting $\epsilon=0$ leads to extremely thin cell—medium interfaces that are

not numerically resolvable. Hence, we adopted a small finite value $\epsilon=0.01$ in the interfacial energy coefficient. Although this choice cannot entirely prevent coarsening, it gives sufficiently slow dynamics and minimizes numerical artefacts. To compare our model with experimental observations (imaged at day 3), we define the simulation

snapshot at $\tilde{t}=2\times10^4$ as a 'quasi-steady state', consistent with the experimental definition at day 3. The model successfully recapitulates key features of monocyte domain formation, including early-stage coalescence and subsequent stabilization of microdomain patterns (Supplementary Video 8). All simulations are run until $\tilde{t}=2\times10^5$, but comparisons with experimental data are based on the quasi-steady state at $\tilde{t}=2\times10^4$ (Supplementary Fig. 2b).

To validate our 'global inhibition' hypothesis, we carried out simulations for the absence of the proposed inhibitory factors by eliminating their production and degradation. With all other parameters fixed at base values, when no inhibitory factors existed in the system, the model degenerated to a typical Cahn–Hilliard model, in which the system displays fewer larger domains, characteristic of macrophase separation at steady state (Fig. 4a). The incorporation of inhibitory factors drove microphase separation due to accumulated inhibitory factors (Supplementary Fig. 2 and Supplementary Video 8). The concentration of global inhibitors depicted in Fig. 4b showed a positive correlation between the concentration of inhibitory factors and cell density, which suggests that the high concentration of inhibitory factors inside the domains lowers the interfacial energy to further stabilize established microdomains.

Next, we assessed the role of 'local activation' modulated via $\beta 2$ integrin–ICAM-1 upregulation (Fig. 2) in our computational model. We adjusted the interfacial energy coefficient $\widetilde{k_3}$ while fixing all other parameters to prove the independence of this parameter's influence on the simulation results. As the $\beta 2$ integrin–ICAM-1 activity decreased, there was a monotonic decrease in the domain size and an increase in the number of domains at steady state (Fig. 4c,d), a sign of insufficient domain formation.

Taken together, we successfully built a Cahn-Hilliard equationbased computational model that closely matched the observed domain formation.

In addition to the concentration \tilde{c} of inhibitory soluble factors and the interfacial energy coefficient k_3 , the cell diffusion coefficient $\widetilde{D_1}$ and the initial cell seeding density $\tilde{\rho}_i$ are two other key parameters in the model that may affect the steady-state simulation results. When gradually tuning down $\overline{D_1}$, the model predicted that the steady-state domain area decreased, while the number of domains increased (Extended Data Fig. 7a,b). Considering that the coefficients (for example, interfacial energy coefficient k_3) in the free energy may be a function of cell seeding density³⁸ and B2 integrin expression was positively correlated with cell density (Supplementary Fig. 3), we increased k_3 correspondingly while increasing the initial cell density $\tilde{\rho}_i$. A monotonic increase in $\widetilde{\rho_i}$ resulted in increased domain area (Extended Data Fig. 7c,d). Interestingly, when a high cell density $\tilde{\rho}_i$ was applied, a relatively consistent domain number was observed at steady state, which indicates that the cell density in each single domain remained constant (Extended Data Fig. 7d).

In the following sections, we describe additional experiments carried out to verify the accuracy of these model predictions.

Influence of cell random motility on domain formation

Similarly to motility-induced phase separation of active matters ^{54,55}, the formation of domains observed in our study was driven by the active movement of monocytes. Immune cell migration has two distinct modes: chemotaxis and random migration ⁵⁸. To understand whether the motility of monocytes could influence domain formation and whether the trend matched the predictions of the model, we treated monocytes with different inhibitors targeting either basal migration or chemotaxis.

Five inhibitors that targeted various cell migration pathways were selected to interfere with monocyte basal random migration, including inhibitors of ROCK (Rho-associated protein kinase), myosin II, Arp2/3, STAT3 and NHE (Na $^+$ /H $^+$ ion exchanger) $^{59-62}$. Inhibitions of ROCK, myosin II and NHE all led to a significant decrease in the average domain area compared (Fig. 5a,b). Accordingly, cell motility was negatively influenced by ROCK and NHE inhibition (Fig. 5c), but no significant difference in domain number was found (Fig. 5d). This indicates that domain size is correlated with cell motility. Consistent with the random migration inhibitor experiments, a decreased diffusion coefficient $\widetilde{D_1}$ resulted in more domains with smaller areas in the simulations (Fig. 5e,f).

To further validate the computational model in which diffusion of monocytes is considered as the sole driving force for domain formation instead of chemotaxis, we used the general chemotaxis inhibitor pertussis toxin, pan-GTPase inhibitor CID-1067700 and the activator of the CCL2-CCR2 axis hCCL2 to target monocyte chemotaxis. For these treatments, monocytes were only found to aggregate into domains of smaller size $(1,522\pm425~\mu\text{m}^2)$ under the influence of pertussis toxin compared with the non-treated control group $(2,007\pm1,020~\mu\text{m}^2)$ (Fig. 5g,h), which also resulted in non-significantly higher domain numbers (Fig. 5i). However, pertussis toxin treatment did not significantly reduce cell movement compared with the control groups (Fig. 5j). These findings suggest that chemotaxis is not a main driving force behind monocyte aggregation and diffusion alone is sufficient to describe monocyte motion in the model.

Onset of domain formation depends on cell seeding density

To eliminate the possibility that the monocyte domain formation was caused by excessive cells in each well, we adjusted the initial cell seeding density in each well. Three different seeding densities –50,000, 25,000 and 10,000 cells per well—were used, which we refer to as high, medium and low densities. On day 1, we observed that monocytes at high cell density formed larger domains $(2,396\pm996~\mu m^2)$ compared with low density $(992\pm423~\mu m^2)$ (Fig. 6a). A linear correlation between the average domain area and cell seeding density was observed (Fig. 6b). Despite variations in initial cell density, we consistently observed the initiation of domain formation across all three density groups (Supplementary Video 9). This suggests that the process of domain formation is independent of the initial monocyte seeding density, as evidenced

$Fig.\,5\,|\,Modulation\,of\,monocyte\,domain\,formation\,by\,cell\,motility.$

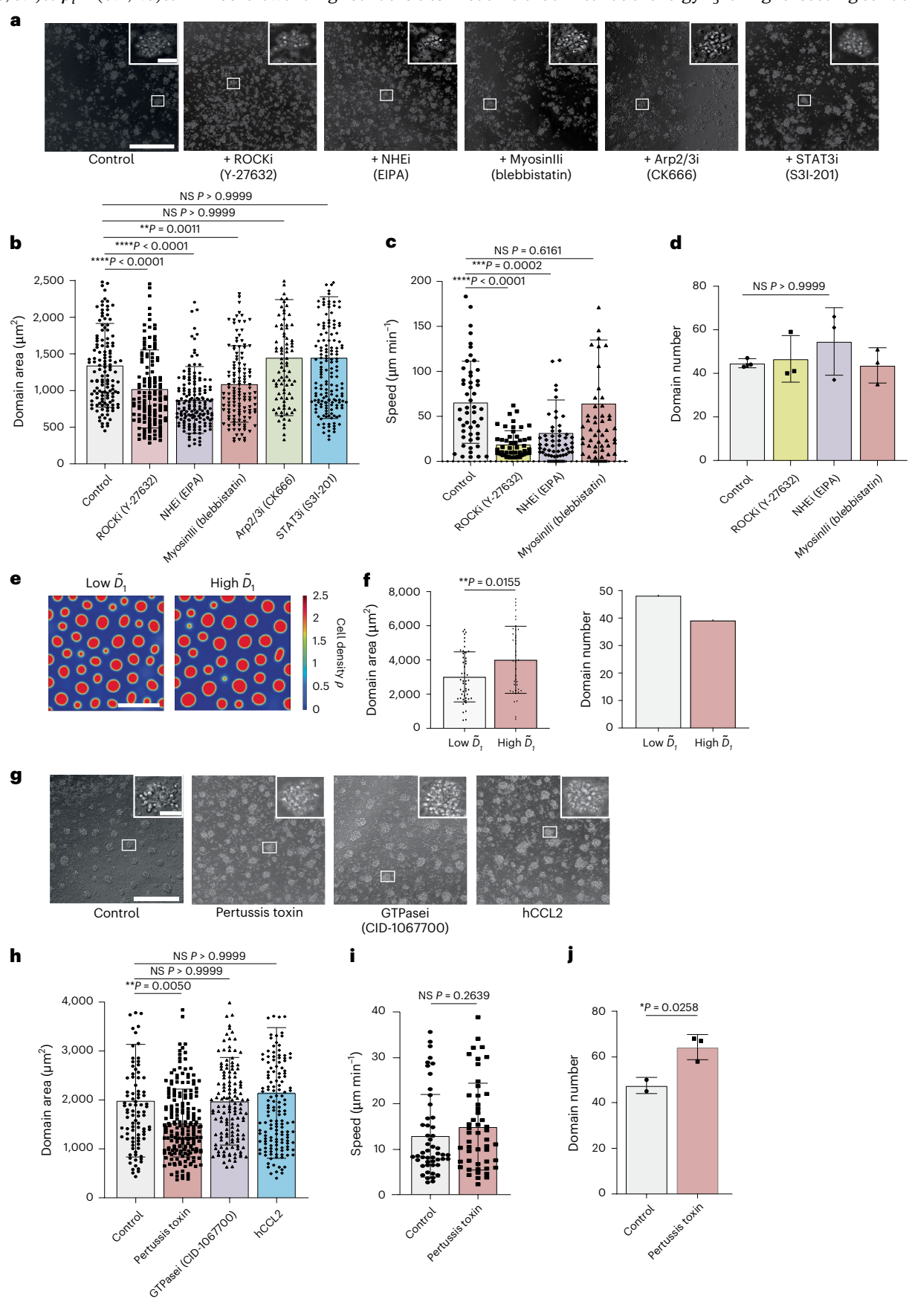
a, Representative images of day 1 monocyte domains treated with various migration inhibitors. \mathbf{b} – \mathbf{d} , Characterization of domain areas with different migration inhibitors: domain area (\mathbf{b}), speed (\mathbf{c}) and domain number (\mathbf{d}). Only conditions that showed significant decrease in domain areas (ROCKi/NHEi/MyosinIIi) were further characterized for single-cell speeds and domain numbers. \mathbf{e} , Simulation results comparing cells of low and high motility. $\widetilde{D_1}$ was chosen as 0.05 for low motility and 0.25 for high motility to reflect the fivefold decrease in cell motility when monocytes were treated with ROCK inhibitor Y-27632. In the simulation, all parameters were fixed except $\widetilde{D_1}$. \mathbf{f} , In the simulation, the domain area decreased in the low-cell-motility group, while low cell motility led to an increase in domain number at steady state. Scale bars, 300 μ m. \mathbf{g} , Representative images of monocyte domain formation when treated with various chemotaxis inhibitors. \mathbf{h} – \mathbf{j} , Characterization of domain areas with

different chemotaxis inhibitors: domain area (**h**), speed (**i**) and domain number (**j**). Only the pertussis toxin group, which showed a significant decrease in domain areas, was further characterized for single-cell speeds and domain numbers. Representative images in **a**, **g** were obtained with a phase-contrast microscope under a $20 \times$ objective. Scale bars, $300 \, \mu m$ and $30 \, \mu m$ (insets). Data in **b**-**d**, **f**, **h**-**j** are presented as mean \pm s.d. with n = 3 independent biological samples (n = 2 for control in **j**, n = 1 for simulation in **f**); all individual domains were measured from three independent biological samples and plotted together in **b**, **c**, **h**, **i**. A Kruskal-Wallis test with Dunn's multiple-comparisons test was used for statistical analysis (*** $P \le 0.001$, *** $P \le 0.001$) in **b**, **c**, **h**, . A two-tailed non-parametric Mann-Whitney test was used for statistical analysis (** $P \le 0.001$) in **d**, **i**, **j**. NS, not significant (P > 0.05).

by the formation of domains even in the low-density group where cells were initially spaced far apart.

In our model, increasing the seeding cell density from $\tilde{\rho_i} \approx (0.6, 0.7)$ to $\tilde{\rho_i} \approx (0.9, 1.0)$ to mimic the low and high cell densities

resulted in a significant increase in domain area (Fig. 6c,d). Our model took into account that $\beta 2$ expression is positively correlated with cell seeding density (Supplementary Fig. 3) and thus we increased the coefficient of interfacial energy \tilde{k}_3 for higher seeding cell density. An



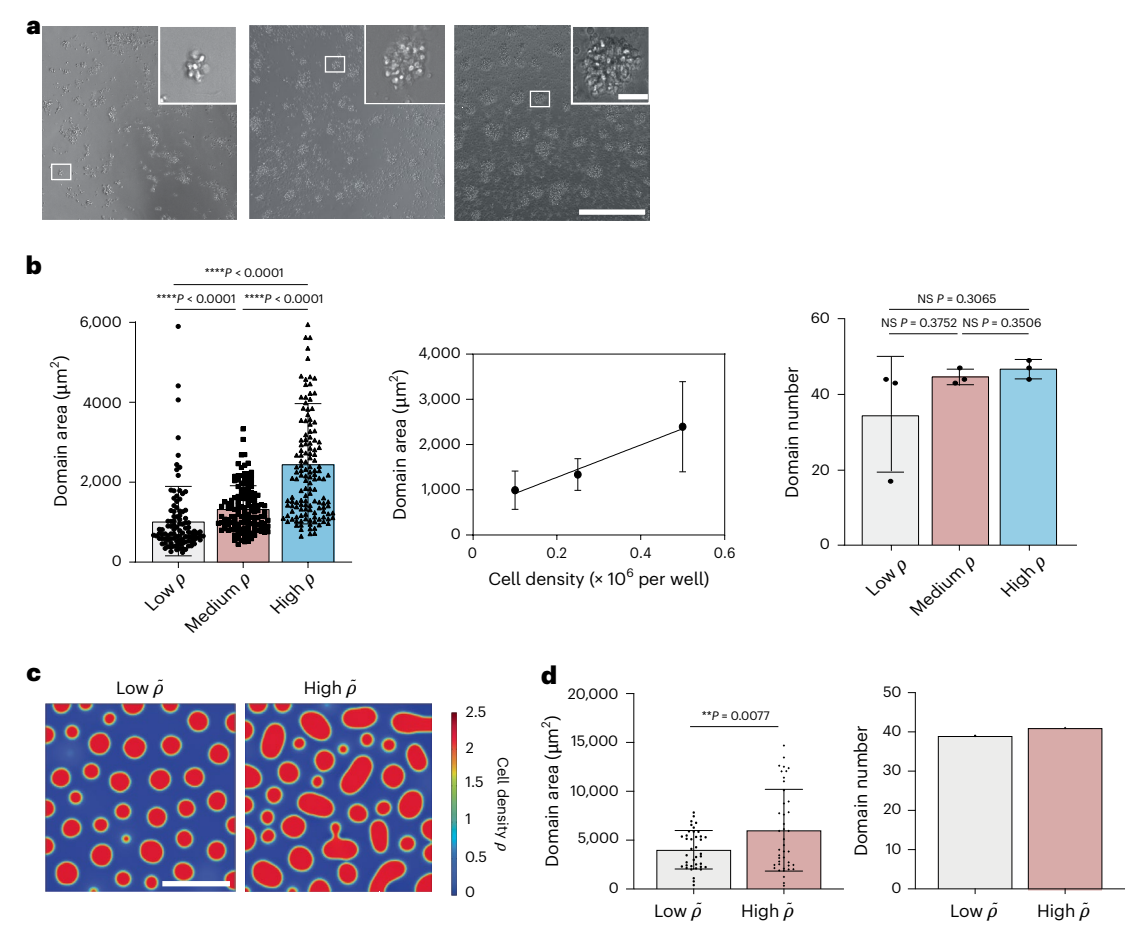


Fig. 6 | Monocyte homotypic domain formation was modulated by local seeding density. a, Representative images of three cell seeding densities captured on day 1. Three cell seeding densities (10,000, 25,000, 50,000 cells per well) representing low (left panel), medium (middle panel), and high (right panel) density were used. b, The average domain area on day 1 exhibited a linear correlation with cell seeding density. Domain numbers remained relatively consistent under different cell seeding densities. c, Steady-state simulation results of low- and high-density groups ($\widetilde{\rho_i} \approx (0.6, 0.7)$ with $\widetilde{k_3} = 0.4$ and $\widetilde{\rho_i} \approx (0.9, 1.0)$ with $\widetilde{k_3} = 2$). All parameters except seeding cell density $\widetilde{\rho_i}$ and interfacial energy coefficient $\widetilde{k_3}$ were fixed. Scale bar, 300 μ m. d, A significant increase of domain area was observed when comparing the high-seeding-density

group condition to the low-seeding-density condition, while the high-density group also exhibited a slight increase in domain number. Representative images in a were obtained with a phase-contrast microscope under a 20× objective. Scale bars, 300 μm and 30 μm (insets). Data in \boldsymbol{b} are presented as mean \pm s.d. with n=3 independent biological samples; all individual domains were measured from three independent biological samples and plotted together in \boldsymbol{b} . A two-tailed non-parametric Mann–Whitney test was used for statistical analysis (**** $P \le 0.0001$) for \boldsymbol{b} (left panel). A two-tailed unpaired t-test with Welch's correction was used for statistical analysis (*** $P \le 0.001$) for \boldsymbol{b} (right panel), \boldsymbol{d} . NS, not significant ($P^>0.05$).

increased domain number was also observed, but the deviation was not large. In general, the simulation results matched well with the experiments with a few concerns that remain to be solved. For example, although the initial diffusible factors concentration \tilde{c} was set at 0, higher seeding cell density introduced a considerable amount of inhibitory soluble factors that might interfere with the steady-state simulation results. A time-delayed introduction of inhibitory soluble factors may offer a better solution for future optimization of the model. Moreover, changes in actomyosin contractility may change the effective adhesion tension and hence the interfacial energy, which should also be included in a future model.

Outlook

To fight against pathogens, monocytes originating from the bone marrow move into the bloodstream and tissues, encountering microenvironments of different stiffnesses. Here, we demonstrate that primary human monocytes respond to differences in stiffness in a way that is unique among major types of immune cells. On matrices of physiological stiffnesses, the ensuing enhanced expression of $\beta 2$ integrin and ICAM-1, which initiates intercellular adhesion, and the secretion

of global inhibitors together produce phase separation, resulting in reversible patterned domain formation.

Monocytes aggregate on matrices of physiological stiffness to enhance their survival, a process that is accompanied with decreased phagocytic capability. This survival scheme is unique to living cells, and different from conventional active matter considered thus far 54,55 . Moreover, self-propelled colloidal particles neither secrete inhibitory molecules, nor actively modulate adhesion molecules on their surface, which are two key ingredients leading to our observed patterned aggregates. Nevertheless, the resemblance between this spontaneous, reversible, patterned aggregation of monocytes and the motility-induced phase separation of active matters motivated us to build a corresponding computational model based on the Cahn–Hilliard equation combined with the Turing model, which reflects the secretion of inhibitory soluble factors and changes in $\beta 2$ integrin–ICAM-1 expressions to bridge active matter phase separation theory to live-cell systems.

Future iterations of the model are required to improve the accuracy of the simulations. For example, time-delayed production of inhibitory factors based on the separation level (for example, the

characteristic distance between adjacent domains) can be applied so that high cell density does not introduce an extremely high level of inhibitory soluble factors that might interfere with the normal initialization of domain formation. Also, since the model is based on an active colloid-like system, cellular complexity and heterogeneity was not fully taken into consideration. Changes in actomyosin contractility could change the effective adhesion tension 63,64 and hence the interfacial energy, which potentially accounts for the lack of any significant difference in the decreased diffusion coefficient $\widetilde{D_1}$ (Fig. 6e). Moreover, aggregated monocytes may exhibit a different secretomic profile compared to actively migrating cells, and the potential effects of layer-stacking domain structure on characteristic domain areas remain unsolved in the current iteration of our model, suggesting the importance of incorporating equations describing related cellular functions.

The term 'microphase separation' has been used in the past to describe isoporous membrane formation driven by amphiphilic block copolymer self-assembly 65,66, biomolecular condensates 67 such as bacterial ribonucleoprotein bodies, RNAP⁶⁸ and FtsZ^{69,70}. The same concept was expanded to living-cell systems mainly describing bacterial microdomains, which are crucial to biofilm formation 71,72. Commonly observed bacterial aggregates of Escherichia coli⁷³ and *Neisseria gonorrhoeae*^{74,75} are driven by chemotactic interactions and are irreversible at steady state when proliferation takes over for further domain development. This fundamentally differs from our observed monocyte phase separation, which is reversible and where random migration is a main driving force, while proliferation shows negligible effects on domain pattern formation. Additionally, the finite size of bacterial domains is often summarized as a consequence of bacterial kinetic slowdown (motility loss) instead of global inhibition induced by secreted factors. More recent studies have focused on eukaryotic cells, such as Dictyostelium discoideum, modelling their non-Turing domain formation by incorporating oxygen availability as long-range repulsion⁷⁶. In contrast, our work develops an experiment-validated Turing computational model that reflects cellular properties and bridges active matter phase-separation theory to live-cell systems.

The biological implications of this work remain to be tested in vivo, but the biophysical mechanism presented here suggests that immune hot-spots can be induced by cells responding to mechanical cues during immune cell trafficking from the peripheral blood to tissues of physiological stiffnesses. The relatively slower kinetics of monocyte domain formation on the 100-kPa substrate also provides exciting insights into tumour onset and progression. Immune hot-spots may be initiated in inflamed soft tissues (1 kPa), not after cancer cells and cancer-associated fibroblasts deposit and cross-link collagen and other extracellular matrix molecules⁷⁷, rendering the tumour matrix stiffer (>25 kPa)⁴⁰.

Online content

Any methods, additional references, Nature Portfolio reporting summaries, source data, extended data, supplementary information, acknowledgements, peer review information; details of author contributions and competing interests; and statements of data and code availability are available at https://doi.org/10.1038/s41563-025-02397-2.

References

- Handorf, A. M., Zhou, Y., Halanski, M. A. & Li, W.-J. Tissue stiffness dictates development, homeostasis, and disease progression. Organogenesis 11, 1–15 (2015).
- Guimarães, C. F., Gasperini, L., Marques, A. P. & Reis, R. L. The stiffness of living tissues and its implications for tissue engineering. Nat. Rev. Mater. 5, 351–370 (2020).
- Selman, M. & Pardo, A. Fibroageing: an ageing pathological feature driven by dysregulated extracellular matrix-cell mechanobiology. *Ageing Res. Rev.* 70, 101393 (2021).

- Sicard, D. et al. Aging and anatomical variations in lung tissue stiffness. Am. J. Physiol. Lung Cell. Mol. Physiol. 314, L946–L955 (2018)
- Phillip, J. M., Aifuwa, I., Walston, J. & Wirtz, D. The mechanobiology of aging. Annu. Rev. Biomed. Eng. 17, 113–141 (2015).
- Chen, H., Cai, Y., Chen, Q. & Li, Z. Multiscale modeling of solid stress and tumor cell invasion in response to dynamic mechanical microenvironment. *Biomech. Model. Mechanobiol.* 19, 577–590 (2020).
- 7. Deng, B. et al. Biological role of matrix stiffness in tumor growth and treatment. *J. Transl. Med.* **20**, 540 (2022).
- Ishihara, S. & Haga, H. Matrix stiffness contributes to cancer progression by regulating transcription factors. Cancers (Basel) https://doi.org/10.3390/cancers14041049 (2022).
- Wirtz, D., Konstantopoulos, K. & Searson, P. C. The physics of cancer: the role of physical interactions and mechanical forces in metastasis. *Nat. Rev. Cancer* 11, 512–522 (2011).
- Nakasaki, M. et al. The matrix protein fibulin-5 is at the interface of tissue stiffness and inflammation in fibrosis. *Nat. Commun.* 6, 8574 (2015).
- Boyette, L. B. et al. Phenotype, function, and differentiation potential of human monocyte subsets. *PLoS One* 12, e0176460 (2017).
- 12. Ginhoux, F. & Jung, S. Monocytes and macrophages: developmental pathways and tissue homeostasis. *Nat. Rev. Immunol.* **14**, 392–404 (2014).
- Wynn, T. A., Chawla, A. & Pollard, J. W. Macrophage biology in development, homeostasis and disease. *Nature* 496, 445–455 (2013).
- Qian, B. Z. et al. CCL2 recruits inflammatory monocytes to facilitate breast-tumour metastasis. *Nature* 475, 222–225 (2011).
- Vijayashankar, D. P. & Vaidya, T. Homotypic aggregates contribute to heterogeneity in B cell fates due to an intrinsic gradient of stimulant exposure. Exp. Cell. Res. 405, 112650 (2021).
- Malet-Engra, G. et al. Collective cell motility promotes chemotactic prowess and resistance to chemorepulsion. *Curr. Biol.* 25, 242–250 (2015).
- Ng, L. G. et al. Visualizing the neutrophil response to sterile tissue injury in mouse dermis reveals a three-phase cascade of events. J. Invest. Dermatol. 131, 2058–2068 (2011).
- O'Flaherty, J. T., Kreutzer, D. L. & Ward, P. A. Neutrophil aggregation and swelling induced by chemotactic agents. J. Immunol. 119, 232–239 (1977).
- Mangaonkar, A. A. et al. Bone marrow dendritic cell aggregates associate with systemic immune dysregulation in chronic myelomonocytic leukemia. *Blood Adv.* 4, 5425–5430 (2020).
- Lefkowitch, J. H., Haythe, J. H. & Regent, N. Kupffer cell aggregation and perivenular distribution in steatohepatitis. *Mod. Pathol.* 15, 699–704 (2002).
- 21. Kiemen, A. L. et al. CODA: quantitative 3D reconstruction of large tissues at cellular resolution. *Nat. Methods* **19**, 1490–1499 (2022).
- 22. de Groot, A. E. et al. Characterization of tumor-associated macrophages in prostate cancer transgenic mouse models. *Prostate* **81**, 629–647 (2021).
- Braxton, A. M. et al. 3D genomic mapping reveals multifocality of human pancreatic precancers. *Nature* 629, 679–687 (2024).
- Kiemen, A. L. et al. 3D histology reveals that immune response to pancreatic precancers is heterogeneous and depends on global pancreas structure. Preprint at bioRxiv https://doi. org/10.1101/2024.08.03.606493 (2024).
- Harjunpää, H., Llort Asens, M., Guenther, C. & Fagerholm, S. C. Cell adhesion molecules and their roles and regulation in the immune and tumor microenvironment. *Front. Immunol.* 10, 1078 (2019).

- Schittenhelm, L., Hilkens, C. M. & Morrison, V. L. β2 integrins as regulators of dendritic cell, monocyte, and macrophage function. Front. Immunol. https://doi.org/10.3389/fimmu.2017.01866 (2017).
- 27. Herter, J. & Zarbock, A. Integrin regulation during leukocyte recruitment. *J. Immunol.* **190**, 4451–4457 (2013).
- Imhof, B. A. & Aurrand-Lions, M. Adhesion mechanisms regulating the migration of monocytes. *Nat. Rev. Immunol.* 4, 432–444 (2004).
- Needleman, D. & Dogic, Z. Active matter at the interface between materials science and cell biology. *Nat. Rev. Mater.* 2, 17048 (2017).
- Vicsek, T., Czirók, A., Ben-Jacob, E., Cohen, I. & Shochet, O. Novel type of phase transition in a system of self-driven particles. *Phys. Rev. Lett.* 75, 1226–1229 (1995).
- 31. Tu, Y. Phases and phase transitions in flocking systems. *Phys. A* **281**, 30–40 (2000).
- 32. Marchetti, M. C. et al. Hydrodynamics of soft active matter. Rev. Mod. Phys. **85**, 1143–1189 (2013).
- Takatori, S. C. & Brady, J. F. Towards a thermodynamics of active matter. Phys. Rev. E 91, 032117 (2015).
- Zhang, J., Alert, R., Yan, J., Wingreen, N. S. & Granick, S. Active phase separation by turning towards regions of higher density. *Nat. Phys.* 17, 961–967 (2021).
- 35. Yan, J. et al. Reconfiguring active particles by electrostatic imbalance. *Nat. Mater.* **15**, 1095–1099 (2016).
- Wu, P.-H., Giri, A., Sun, S. X. & Wirtz, D. Three-dimensional cell migration does not follow a random walk. *Proc. Natl Acad. Sci.* USA 111, 3949–3954 (2014).
- 37. Li, B. & Sun, S. X. Coherent motions in confluent cell monolayer sheets. *Biophys. J.* **107**, 1532–1541 (2014).
- Cahn, J. W. & Hilliard, J. E. Free energy of a nonuniform system. I. Interfacial free energy. J. Chem. Phys. 28, 258–267 (2004).
- 39. Lee, D. et al. Physical, mathematical, and numerical derivations of the Cahn–Hilliard equation. *Comput. Mater. Sci.* **81**, 216–225 (2014).
- Sneider, A. et al. Deep learning identification of stiffness markers in breast cancer. *Biomaterials* 285, 121540 (2022).
- Martino, F., Perestrelo, A. R., Vinarský, V., Pagliari, S. & Forte, G. Cellular mechanotransduction: from tension to function. *Front. Physiol.* https://doi.org/10.3389/fphys.2018.00824 (2018).
- Du, H. et al. Tuning immunity through tissue mechanotransduction. Nat. Rev. Immunol. 23, 174–188 (2023).
- Shemesh, T., Geiger, B., Bershadsky, A. D. & Kozlov, M. M. Focal adhesions as mechanosensors: a physical mechanism. *Proc. Natl Acad. Sci.* 102, 12383–12388 (2005).
- 44. Kim, D.-H. et al. Actin cap associated focal adhesions and their distinct role in cellular mechanosensing. *Sci. Rep.* **2**, 555 (2012).
- Wu, Z., Plotnikov, S. V., Moalim, A. Y., Waterman, C. M. & Liu, J. Two distinct actin networks mediate traction oscillations to confer focal adhesion mechanosensing. *Biophys. J.* 112, 780–794 (2017).
- Dupont, S. et al. Role of YAP/TAZ in mechanotransduction. *Nature* 474, 179–183 (2011).
- Panciera, T., Azzolin, L., Cordenonsi, M. & Piccolo, S. Mechanobiology of YAP and TAZ in physiology and disease. *Nat. Rev. Mol. Cell Biol.* 18, 758–770 (2017).
- Wang, C. et al. Verteporfin inhibits YAP function through up-regulating 14-3-3σ sequestering YAP in the cytoplasm. Am. J. Cancer Res 6, 27–37 (2016).
- Kasinrerk, W., Tokrasinwit, N. & Phunpae, P. CD147 monoclonal antibodies induce homotypic cell aggregation of monocytic cell line U937 via LFA-1/ICAM-1 pathway. *Immunology* 96, 184–192 (1999).

- Campanero, M. R. et al. An alternative leukocyte homotypic adhesion mechanism, LFA-1/ICAM-1-independent, triggered through the human VLA-4 integrin. J. Cell Biol. 110, 2157–2165 (1990).
- 51. Flo, T. H. et al. Involvement of CD14 and β2-integrins in activating cells with soluble and particulate lipopolysaccharides and mannuronic acid polymers. *Infect. Immun.* **68**, 6770–6776 (2000).
- Lecoanet-Henchoz, S. et al. CD23 Regulates monocyte activation through a novel interaction with the adhesion molecules CD11b-CD18 and CD11c-CD18. *Immunity* 3, 119–125 (1995).
- 53. Oberyszyn, T. M. et al. β2 integrin/ICAM-1 adhesion molecule interactions in cutaneous inflammation and tumor promotion. *Carcinogenesis* **19**, 445–455 (1998).
- 54. Gonnella, G., Marenduzzo, D., Suma, A. & Tiribocchi, A. Motility-induced phase separation and coarsening in active matter. C. R. Phys. **16**, 316–331 (2015).
- 55. Cates, M. E. & Tailleur, J. Motility-induced phase separation. *Annu. Rev. Condens. Matter Phys.* **6**, 219–244 (2015).
- Maini, P. K., Woolley, T. E., Baker, R. E., Gaffney, E. A. & Lee,
 S. S. Turing's model for biological pattern formation and the robustness problem. *Interface Focus* 2, 487–496 (2012).
- 57. Steinfeld, J. I., Francisco, J. S. & Hase, W. L. Chemical kinetics and Dynamics (Prentice Hall, 1999).
- 58. Du, W., Nair, P., Johnston, A., Wu, P.-H. & Wirtz, D. Cell trafficking at the intersection of the tumor–immune compartments. *Annu. Rev. Biomed. Eng.* **24**, 275–305 (2022).
- 59. Jayatilaka, H. et al. Synergistic IL-6 and IL-8 paracrine signalling pathway infers a strategy to inhibit tumour cell migration. *Nat. Commun.* **8**, 15584 (2017).
- 60. Stroka, K. M. Water permeation drives tumor cell migration in confined microenvironments. *Cell* **157**, 611–623 (2014).
- 61. Bera, K. et al. Extracellular fluid viscosity enhances cell migration and cancer dissemination. *Nature* **611**, 365–373 (2022).
- 62. Giri, A. et al. The Arp2/3 complex mediates multigeneration dendritic protrusions for efficient 3-dimensional cancer cell migration. *FASEB J.* **27**, 4089–4099 (2013).
- Maghzal, N., Kayali, H. ulyaA., Rohani, N., Kajava, A. ndreyV. & Fagotto, F. EpCAM controls actomyosin contractility and cell adhesion by direct inhibition of PKC. Dev. Cell 27, 263–277 (2013).
- Clark, K. et al. TRPM7, a novel regulator of actomyosin contractility and cell adhesion. *EMBO J.* 25, 290-301–290-301 (2006).
- 65. Bates, F. S. et al. Multiblock polymers: panacea or Pandora's box?. *Science* **336**, 434–440 (2012).
- 66. Peinemann, K.-V., Abetz, V. & Simon, P. F. W. Asymmetric superstructure formed in a block copolymer via phase separation. *Nat. Mater.* **6**, 992–996 (2007).
- 67. Azaldegui, C. A., Vecchiarelli, A. G. & Biteen, J. S. The emergence of phase separation as an organizing principle in bacteria. *Biophys. J.* **120**, 1123–1138 (2021).
- Nandana, V. & Schrader, J. M. Roles of liquid-liquid phase separation in bacterial RNA metabolism. *Curr. Opin. Microbiol.* 61, 91–98 (2021).
- 69. Monterroso, B. et al. Bacterial FtsZ protein forms phase-separated condensates with its nucleoid-associated inhibitor SlmA. *EMBO Rep.* **20**, e45946 (2019).
- Lan, G., Daniels, B. R., Dobrowsky, T. M., Wirtz, D. & Sun, S. X. Condensation of FtsZ filaments can drive bacterial cell division. *Proc. Natl Acad. Sci. USA* 106, 121–126 (2009).
- 71. Hall-Stoodley, L., Costerton, J. W. & Stoodley, P. Bacterial biofilms: from the natural environment to infectious diseases. *Nat. Rev. Microbiol.* **2**, 95–108 (2004).
- Ghosh, P., Mondal, J., Ben-Jacob, E. & Levine, H. Mechanically-driven phase separation in a growing bacterial colony. *Proc. Natl Acad. Sci. USA* 112, E2166–E2173 (2015).

- Budrene, E. O. & Berg, H. C. Dynamics of formation of symmetrical patterns by chemotactic bacteria. *Nature* 376, 49–53 (1995).
- 74. Taktikos, J., Lin, Y. T., Stark, H., Biais, N. & Zaburdaev, V. Pili-induced clustering of *N. gonorrhoeae* bacteria. *PLoS One* **10**, e0137661 (2015).
- 75. Kuan, H.-S., Pönisch, W., Jülicher, F. & Zaburdaev, V. Continuum theory of active phase separation in cellular aggregates. *Phys. Rev. Lett.* **126**, 018102 (2021).
- Carrère, A. et al. Microphase separation of living cells. Nat. Commun. 14, 796 (2023).
- 77. Gilkes, D. M., Semenza, G. L. & Wirtz, D. Hypoxia and the extracellular matrix: drivers of tumour metastasis. *Nat. Rev. Cancer* **14**, 430–439 (2014).

Publisher's note Springer Nature remains neutral with regard to jurisdictional claims in published maps and institutional affiliations.

Springer Nature or its licensor (e.g. a society or other partner) holds exclusive rights to this article under a publishing agreement with the author(s) or other rightsholder(s); author self-archiving of the accepted manuscript version of this article is solely governed by the terms of such publishing agreement and applicable law.

@ The Author(s), under exclusive licence to Springer Nature Limited 2025

Methods

Isolation and culture of human primary monocytes/B cells/NK cells/T cells

Peripheral blood mononuclear cells (PBMCs) were isolated from donors' whole blood by Ficoll-paque PLUS (Cytiva, 17144003) density gradient centrifugation. First, 5 ml of blood from leukopak was pipetted into each 50-ml conical tube. RPMI (Gibco, 11875) was added to raise the volume in each conical tube to 35 ml. Then, 13 ml of Ficoll-paque PLUS medium was slowly pipetted underneath the blood/RPMI mixture without disturbance at the interface. Conical tubes were centrifuged at 400g for 30 min with the brake turned off. Mononuclear cell layers were then harvested from each conical tube, combined and PBMCs were counted using a haemacytometer. Isolated PBMCs were aliquoted and frozen at 5×10^7 cells per cryovial in freezing medium consisting of 90% fetal bovine serum (Corning, 35-010-CV) and 10% dimethylsulfoxide (ATCC, 4-X-5).

Human primary classical monocytes (CD14⁺CD16⁻) were further isolated using the Classical Monocyte Isolation Kit (Miltenyi Biotec, 130-117-337) by magnetic-activated cell sorting following the manufacturer's protocol. Human CD14⁺CD16⁻ monocytes were resuspended in DMEM (Corning, 10-013-CV) supplemented with 10% v/v heat-inactivated fetal bovine serum (Corning, 35-010-CV) and 1% v/v penicillin-streptomycin (Sigma, P4333). Monocytes were cultured at a density of 0.5×10^6 cells per well and incubated at 37 °C; 96-well culture plates, either standard tissue culture plastic/glass-coated with collagen I or Softwell 96-well plates (Matrigen, SW96-COL-0.5/100) containing collagen I-coated polyacrylamide gel with stiffness values of 0.5 and 100 kPa, were used. Similarly, human primary B cells/NK cells/T cells were isolated from donor PBMCs using corresponding isolation kits (B cell, STEMCELL 17954; NK cell, STEMCELL 17955; T cell, STEMCELL 17911) per the manufacturer's protocol. B cells were cultured in ImmunoCult-XF B cell base medium (STEMCELL, 100-0646) with B-cell expansion supplement (STEMCELL, 10974). NK cells were cultured in ImmunoCult NK cell base medium (STEMCELL, 100-0712) with NK cell expansion supplement (STEMCELL, 100-0715). B cells and NK cells were activated with 200 U ml⁻¹ IL-2 (PeproTech, 200-02). T cells were cultured in X-VIVO 15 medium (Lonza, 02-060Q) with 5% human AB serum (Millipore Sigma, H4522), 2 mM L-glutamine (Gibco, 25030081), and 100 U ml⁻¹ penicillin and 100 mg ml⁻¹ streptomycin (Gibco, 15140122). T cells were activated with 100 U ml⁻¹ IL-2 (PeproTech, 200-02) and CD3/CD28 T-cell activator (STEMCELL, 10971). Macrophages were differentiated from negatively isolated human primary monocytes in macrophage attachment medium-DMEM (Corning, 10-013-CV) supplemented with 10% v/v heat-inactivated fetal bovine serum (Corning, 35-010-CV), 1% v/v penicillin-streptomycin (Sigma, P4333) and 50 ng ml⁻¹human recombinant macrophage colony-stimulating factor (R&D, 216-MC). Monocytes were seeded at a density of 2.5×10^6 in each well of a standard six-well tissue-culture plate $(5 \times 10^6 \text{ monocytes per well})$ in macrophage attachment medium the day they were isolated from donor PBMCs. After 3 days, cells remaining in suspension were gently aspirated away and fresh macrophage attachment medium was added. Macrophages were ready to be harvested and seeded after 7 days of differentiation, when they were regarded as MO naïve macrophages.

Collagen I coating of tissue-culture plates

Based on the previously described method, low-concentration collagen I (Corning, 354236) was diluted with 0.1% acetic acid (Fisher Chemical, A38-212) in PBS (Gibco, 14190-144) to a final concentration of $100~\mu g~ml^{-1}$. Then, 96-well plastic cell culture plates were washed with PBS three times before adding 32 μ l of diluted collagen I per well. After 1 h of incubation, the excess liquid in each well was aspirated out carefully, followed by PBS washing. Complete DMEM was used to condition the plate for 1 h before use.

Blockage of monocyte mechanosensing and transduction

To explore whether the observed monocyte homotypic domain

formation on matrices of physiological stiffness is mechano-induced, $20~\mu\text{M}$ of focal adhesion kinase inhibitor Y15 (Selleckchem, S5321), 200~nM of F-actin network destabilizer latrunculin A (Cayman Chemical, 10010630) and $1~\mu\text{M}$ of YAP/TAZ inhibitor verteporfin (MedChem-Express, HY-B0146) were added to the cell culture medium during the monocyte monolayer seeding.

Antibody-based inhibition and activation of monocyte cell-surface integrins

To explore the cell-surface molecule engaged in the domain formation process, 6.25 μg ml $^{-1}$ blocking antibodies against integrin $\beta 2$ (clone TS1/18, Biolegend, 302102) and 6.25 μg ml $^{-1}$ activation antibodies against integrin $\beta 2$ (clone m24 and LFA-1/2, Biolegend, 363402 and 366302) were added to the cell culture medium at the start of the culture. Functional blocking of cell-surface ICAM-1, integrin $\alpha 4$ and integrin αM was carried out via treated monocytes in medium with 6.25 μg ml $^{-1}$ anti-CD54 antibody (clone HA58, Biolegend, 353102), 6.25 μg ml $^{-1}$ anti-CD49d antibody (clone M1/70.15, Invitrogen, MA1-80091).

Chemical inhibition of monocyte migration

Isolated human CD14 $^+$ CD16 $^-$ monocytes were incubated with various inhibitors upon seeding. Several inhibitors were used to interfere with the random migration of monocytes: 20 μ M RhoA Kinase ROCK inhibitor Y-27632 (Selleckchem, S6390), 100 μ M Arp inhibitor CK666 (Selleckchem, S7690), 100 μ M STAT3 inhibitor S3I-201 (Selleckchem, S1155), 10 μ M blebbistatin for non-muscle myosin II inhibition (Millipore Sigma, B0560) and 10 μ M EIPA (Millipore Sigma, A3085) to block the sodium–hydrogen exchanger (NHE). Monocytes were incubated with 2 μ g ml $^{-1}$ pertussis toxin (EMD Millipore Crop, 516560), 20 μ M CID-1067700 (MedChemExpress, HY-13452) and 2 μ g ml $^{-1}$ recombinant human CCL2 (Biolegend, 571402).

PrestoBlue cell-viability assay

A 2× working solution of PrestoBlue (Invitrogen, A13261) was prepared by mixing $10\times$ stock solution to complete DMEM at a ratio of 1:5. Then, $100~\mu l$ of medium was gently aspirated from each testing well of a 96-well plate (200 μl in total) and $100~\mu l$ of 2× working solution was added slowly to avoid any agitation to the monocyte domains. After 3 h of incubation in a 37 °C, 5% CO $_2$ incubator, the plate was wrapped in aluminium foil and transferred to a SpectraMax M3 plate reader (Molecular Devices). Fluorescence signals were read at an excitation of 560 nm and an emission of 590 nm. Cell-viability data were acquired using Molecular Devices SoftMAX Pro v.7 software.

Flow cytometry

Fluorescence-activated cell sorting (FACS) wash buffer was made with PBS (Gibco, 14190-144) containing 2% v/v FBS (Corning, 35-010-CV), 1 mM EDTA (Invitrogen, 15575020) and 0.1% w/v NaN₃ (Sigma, S8032). Cell samples were washed three times in PBS and resuspended at a concentration of 10⁷ cells ml⁻¹ in 100 μl. Cell suspensions were blocked with 5 µl of Human TruStain FcX (Biolegend, 422301) for 15 min under room temperature. The antibodies (5 µl per antibody for 1 million cells) were then added and incubated at 4 °C for 30 min, protected from light. Antibodies used for cell labelling were as follows: APC anti-human CD18 (clone TS1/18, Biolegend, 302113), PE anti-human CD54 (clone HA58, Biolegend, 353105). For unstained control sample, isotype antibodies of APC Mouse IgG1, κ Isotype Ctrl (Biolegend, 400121) and PE Mouse IgG1, κ Isotype Ctrl (Biolegend, 400112) were applied (5 μl per antibody for 1 million cells). Cells were washed with 3 ml of FACS wash buffer and then resuspended in 350 µl FACS wash buffer. For the cell-viability assay, cells were washed three times in PBS and resuspended in $500\,\mu l$ of FACS wash buffer. Then, 10 µl of propidium iodide solution (Biolegend, 421301) was added and samples were incubated at 4 °C for 15 min,

protected from light. Immunofluorescence-stained cells were analysed on a FACS Canto. Analysis was performed with Flowjo v.10.4 software. The cell-surface marker mean fluorescence intensity of each sample was corrected with the mean fluorescence intensity measured for the corresponding isotype control.

Gene expression analysis using RT-qPCR

Total RNA from monocytes subjected to different stiffness conditions and culture times was isolated using an RNeasy Micro Kit (Qiagen, 74004). cDNA synthesis was performed using iScript cDNA Synthesis Kit (Bio-Rad, 1708890). Real-time PCR reactions were set up using iTaq Universal SYBR Green Supermix (Bio-Rad, 1725121) and were executed in a thermal cycler (CFX384 Real-Time System, Bio-Rad). The primers designed for specific gene amplification are listed in Supplementary Table 1. Relative quantitation was performed using the $\Delta\Delta$ Ct method in CFX Manager v.3.1 software.

Western blot

Whole-cell protein lysates were prepared in clear sample buffer (0.5 M Tris pH 6.8, 20% SDS, 50% glycerol in water). Total protein concentration was evaluated using a Micro BCA Protein Assay Kit (Thermo Scientific, 23235). Based on the calculation, 20 µg total proteins from different samples were loaded on 4-15% SDS-PAGE gel (Bio-Rad, 4561086) and ran in 1× Tris/glycine/SDS buffer (Bio-Rad 1610772) at a voltage of 180 V under room temperature for electrophoresis. Protein bands were transferred to polyvinylidene difluoride membrane using the Trans-Blot Turbo system (Bio-Rad, 17001919). TBST buffer was made by supplementing 1× TBS buffer (Bio-Rad 1706435) with 0.1% v/v Tween 20 (Sigma, P7949). The membrane was blocked in TBST with 5% dry milk (Bio-Rad, 1706404) for 60 min at room temperature and incubated with primary antibodies at 4 °C for overnight. After washing three times with TBST, the membrane was incubated with secondary antibodies for 60 min at room temperature. Then, after washing three times in TBST, 1 ml of ECL substrate solution (Prometheus, 20-302) was added to the membrane and incubated for 2 min. The membrane was then analysed using a ChemiDoc XRS+ imaging system (Bio-Rad). Images were analysed using Image Lab v.6.0 software. The intensity of the targeted protein band was normalized using housekeeping protein. Primary and secondary antibodies were used as follows: GAPDH (14C10) rabbit mAb (CST, 2118S), integrin β2 (D4N5Z) rabbit mAb (CST, 73663S), anti-rabbit IgG HRP-linked antibody (CST, 7074S), Primary antibodies were diluted 1:1,000 in TBST with 1% milk and secondary antibody was diluted 1:5,000 in TBST with 5% dry milk for staining.

Conditioned medium preparation and treatment

Atotal of 50,000 cells were seeded into each well of the 0.5-kPa/100-kPa/plastic/glass 96-well plates. Conditioned medium was harvested from each well after 24 h of incubation. Harvested supernatant was centrifuged at 300g for 5 min and passed through a 0.22- μ m polyether sulfone (PES) filter (Genesee, 25-244) to eliminate any possible cells in it. Aliquots of conditioned medium were stored in a $-80\,^{\circ}\text{C}$ freezer until use. Different dilutions of conditioned medium were prepared by mixing the conditioned medium with fresh DMEM in different volume ratios for further monocyte culture on 0.5-kPa substrate.

Ultracentrifugation

Conditioned media were harvested from monocytes seeded on different substrates (plastic and 0.5 kPa) on day 1 and filtered through 0.22- μ m PES filters (Genesee, 25-244). Conditioned media were then concentrated at 14,000 g for 10 min using Amicon Ultra centrifugal filter units with a 10-kDa molecular weight cut-off (Millipore Sigma, UFC8010). Flowthrough (contains monocyte-secreted small molecules) and concentrate (contains monocyte-secreted proteins) of the conditioned medium were then harvested and diluted back to original volume before ultracentrifugation with fresh DMEM.

Sample processing for protein extraction and tryptic digestion

Each sample's conditioned medium was concentrated at 14.000g for 10 min using Amicon Ultra centrifugal filter units with a 10-kDa molecular weight cut-off (Millipore Sigma, UFC8010). Following concentration, protein precipitation was performed using prechilled acetone at -20 °C, with the acetone volume being four times that of the concentrated conditioned medium. After acetone precipitation, the proteins were processed using the S-trap method (Protifi), following the manufacturer's instructions. Briefly, the proteins were reduced, alkylated and then digested with trypsin and LysC in the S-Trap microcolumn. The trapped peptides were eluted from the column using 50 mM triethylammonium bicarbonate (TEAB), 0.2% formic acid and 50% acetonitrile. The peptides were dried using Speed-Vac (Thermo Scientific) and reconstituted with 0.1% formic acid. Finally, 1 ug of peptides was loaded onto an Evotip (Evosep Biosystems) according to the EvosepOne (Evosep Biosystems) protocol for global proteomic analysis on a timsTOF-HT (Bruker, 4th generation).

Evosep-timsTOF for global proteomic analysis

All the liquid chromatography tandem mass spectrometry (LC–MS/MS) data were acquired via Evosep coupled with a timsTOF-HT (Bruker) in data-independent acquisition mode. The methods for acquiring global proteomics are as follows. Global peptides were loaded on an Evotip and separated on a PepSep C18 column of 15 cm × 150 μ m, 1.5 μ m (Bruker) in a Bruker column toaster (50 °C) at a 30 sample per day (SPD) gradient. The global proteomic data were acquired using the data-independent acquisition parallel accumulation serial fragmentation (DIA-PASEF) mode on the timsTOF-HT with the following settings: MS1 scan range, 100–1,700 m/z; MS2 scan range, 338–1,338 m/z; mass width, 25.0 Da without mass overlap; 1 mobility window; $1/K_0$ range, 0.70–1.45 V s cm⁻²; ramp time, 85.0 ms.

Mass spectrometry data analysis

All the raw files were searched against the UniProt/Swiss-Prot database containing human proteins (downloaded on 7 February 2024, 20,433 entries) using the direct data-independent acquisition (directDIA) approach in Spectronaut v.18 (Biognosys). The search setting is as follows. The mass tolerance of MS and MS/MS was set as dynamic with a correction factor of 1. Precursors were filtered by a Q-value cut-off of 0.01 (which corresponds to a false discovery rate of 1%). Carbamidomethyl (C) was set as a fixed modification. Acetyl (protein N-term) and Oxidation (M) were set as variable modifications. Carbamidomethyl (C) refers to the modification of cysteine residues. Acetyl (protein N-term) indicates acetylation at the protein's N-terminus. Oxidation (M) refers to methionine oxidation. The quantity of a peptide was a sum of the quantity of its top three precursors, whereas the quantity for a precursor was calculated by summing the area of its top three fragment ions at the MS/MS level. The data were normalized by dividing them by the median of each sample. Missing values are filled with half of the minimum value of the entire data. Differential analysis was carried out by calculating the mean log₂ fold changes between the plastic and 0.5-kPa groups and a two-tailed Student's t-test was performed to obtain P-values.

Live-cell staining and phagocytosis assay

Monocytes were labelled using Cell Tracker CMTPX dye (Invitrogen, C34552) at a working concentration of 5 μ M for 15 min in an incubator immediately before seeding. After 1 day of incubation, cells inside and outside the domains were separated by gentle pipetting and TrypLE (Gibco, 12604013) detachment. These two portions of the cells were seeded to a new plastic plate at a density of 10,000 cells per well. Carboxylate-modified polystyrene fluorescent beads (Sigma, L4655), 1 μ min diameter, were added to the cells at a concentration of 5 beads per cell. Fluorescence images were taken every 30 min for 6 h. The merged images were obtained to count the total number of beads per cell.

Live-cell imaging and cell tracking

Human classical (CD14⁺CD16⁻) monocytes were seeded at 50,000 cells per well on collagen I-coated 96-well plates for domain formation. After seeding, plates were centrifuged at 12g for 5 min to form a monocyte monolayer. Images were taken every 1 min for 6 h using a Nikon Eclipse Ti2 equipped with a stage top incubator. For cell motility analysis, monocytes were seeded at a lower density of 25,000 cells per well to ensure more accurate tracking via software. Cell motilities were analysed using MetaMorph and MATLAB. To ensure the accuracy of manual tracking, >50 cells in each field of view were analysed.

Finite-element method simulation

The computational model based on the Cahn–Hilliard equation was numerically solved using the commercial finite-element method software COMSOL Multiphysics 6.0. The original partial differential equations (PDE) set was rewritten in the weak form and solved on a square domain with dimensionless side length $\tilde{l}=100$. For spatial discretization, we use a free triangular mesh with a maximum element size of 2 and a minimum element size of 0.0075. We chose the cubic Hermite shape function for the finite-element method analysis. For the discrete time-stepping scheme, we used the implicit backward differentiation formula (BDF) method.

Statistics and reproducibility

Graphpad Prism v.10.0.0 was used for statistical analysis. An unpaired Student's t-test with Welch's correction was performed to evaluate the statistical significance between two groups for characterized domain number data. A non-parametric Mann–Whitney U-test was performed to evaluate the statistical significance between two groups for characterized domain area data. An unpaired Student's t-test was performed to evaluate the statistical significance between two groups for characterized domain number data. For column analysis of multiple conditions, Kruskal–Wallis with Dunn's multiple-comparisons test was performed. Significant values are given in grades: $*P \le 0.05$, $**P \le 0.01$, $****P \le 0.001$, $****P \le 0.0001$.

All experiments were tested using cells from multiple independent donors. Key findings were consistent across donors, minimizing the impact of donor-to-donor variability. Covariates related to donor variability were inherently controlled by replication across different donors. No statistical method was used to predetermine sample size. No data were excluded from analysis. Investigators were blinded to group allocation during experiments involving blood samples.

Reporting summary

Further information on research design is available in the Nature Portfolio Reporting Summary linked to this article.

Data availability

The data supporting the findings of this work are available within the Article and its Supplementary Information. The proteomics raw data

are available via PRIDE at https://www.ebi.ac.uk/pride/ with the accession number PXD063197. Source data are provided with this paper.

Code availability

The simulations were performed with the commercial software Multiphysics v. 6.1 (COMSOL). No custom code or external scripts were used. The Multiphysics (.mph) model files used in the simulations reported in the manuscript are available via Zenodo at https://doi.org/10.5281/zenodo.17247622 (ref. 78).

References

 Wu, Y. & Du, W. Computational model to simulate mechano-induced patterned domain formation by monocytes. Zenodo https://doi.org/10.5281/zenodo.17247622 (2025).

Acknowledgements

The authors thank the members of the Wirtz and Sun labs for their feedback. This work was supported through grants to D.W. from the National Cancer Institute (U54CA268083 and RO1CA300052) and the National Institute on Aging (U01AG060903).

Author contributions

D.W. and W.D. conceptualized this project. W.D. and J.Z. designed and carried out the experiments. H.L. performed the proteomics. Different types of immune cells were provided by Z.W. and E.A.H. Y.W. developed the model and carried out the simulations with input from S.X.S. Data in Supplementary Fig. 1a,b were collected and analysed by A.L.K. with input from D.W. The manuscript was written by W.D. and Y.W. with edits and input from D.W., S.X.S., A.L.K., H.Z. and J.Z.

Competing interests

The authors declare no competing interests.

Additional information

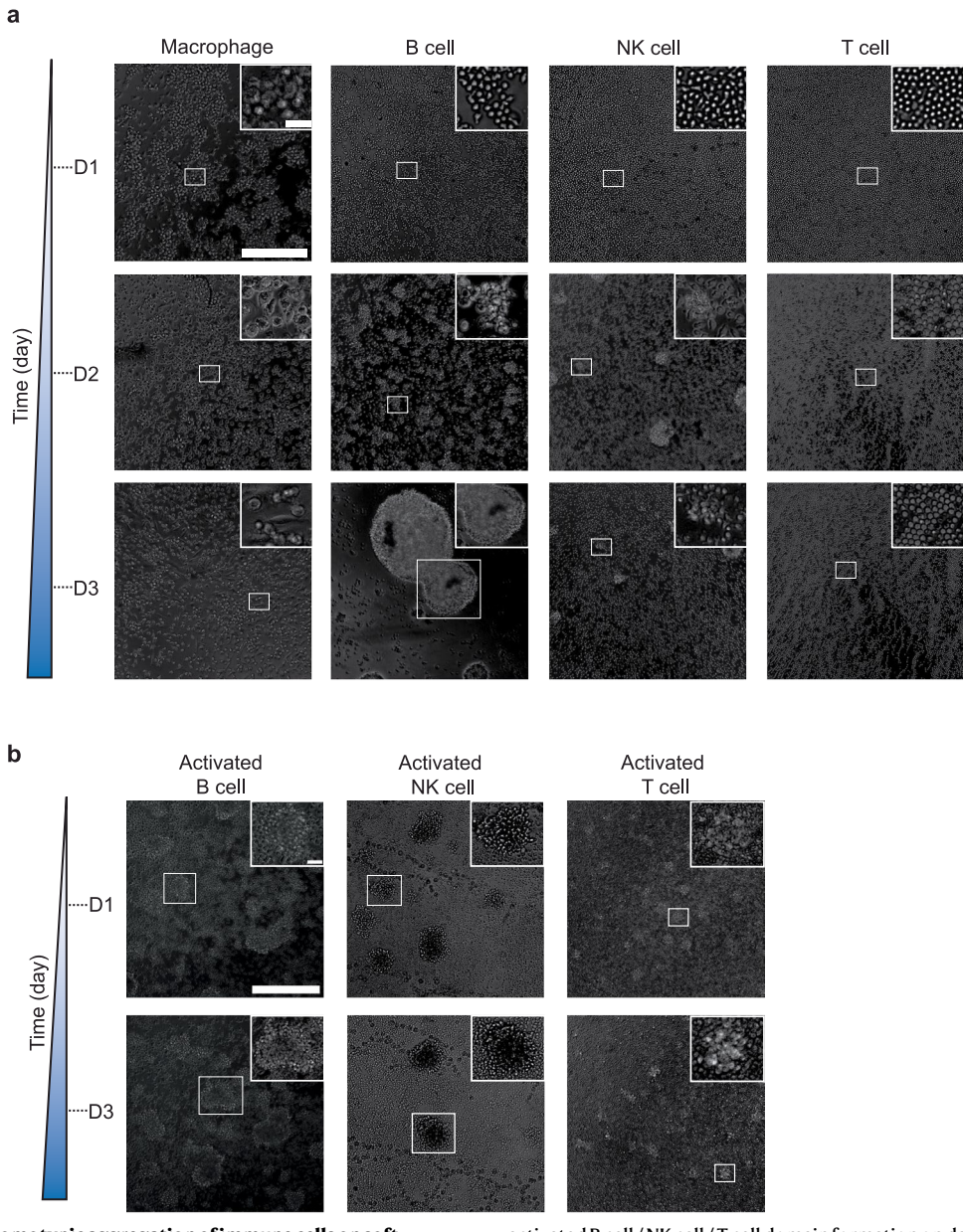
Extended data is available for this paper at https://doi.org/10.1038/s41563-025-02397-2.

Supplementary information The online version contains supplementary material available at https://doi.org/10.1038/s41563-025-02397-2.

Correspondence and requests for materials should be addressed to Sean X. Sun or Denis Wirtz.

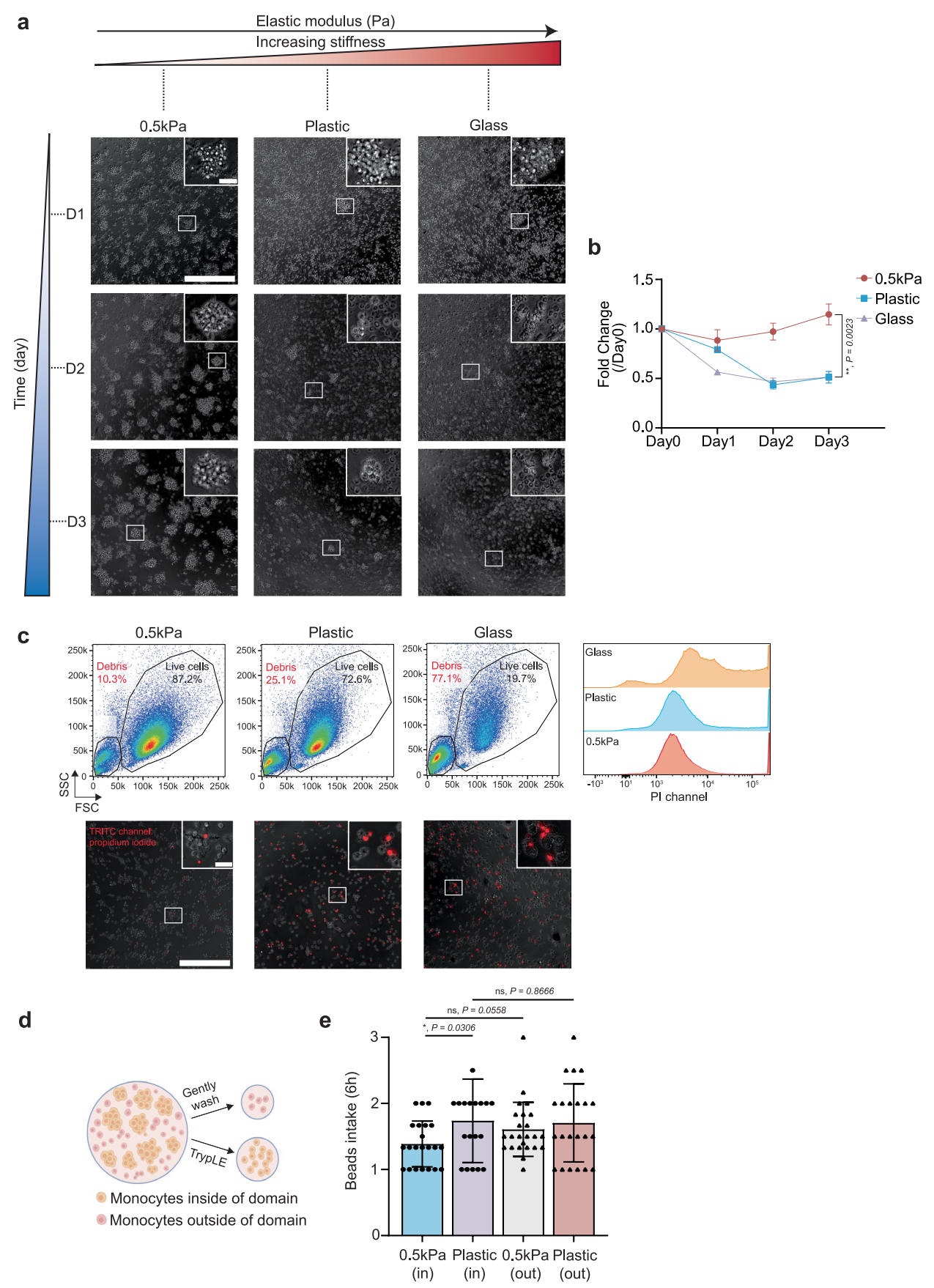
Peer review information *Nature Materials* thanks Johanna Ivaska and the other, anonymous, reviewer(s) for their contribution to the peer review of this work.

Reprints and permissions information is available at www.nature.com/reprints.



Extended Data Fig. 1 | Homotypic aggregation of immune cells on soft substrates. a, Representative 20x phase-contrast images of macrophages / B cell / NK cell / T cell domain formations on collagen I-coated 0.5kPa substrate obtained on day 1, day 2 and day 3. None of the lymphocytes (B cells, T cells, and NK cells) initiated homotypic aggregation for the first 24 h. Macrophages, however, displayed homotypic aggregation on day 1 but failed to maintain it. Representative day 1 images were taken with a 10x objective, while day 2/3 images were taken with a 20x objective. b, Representative 20x phase contrast images of

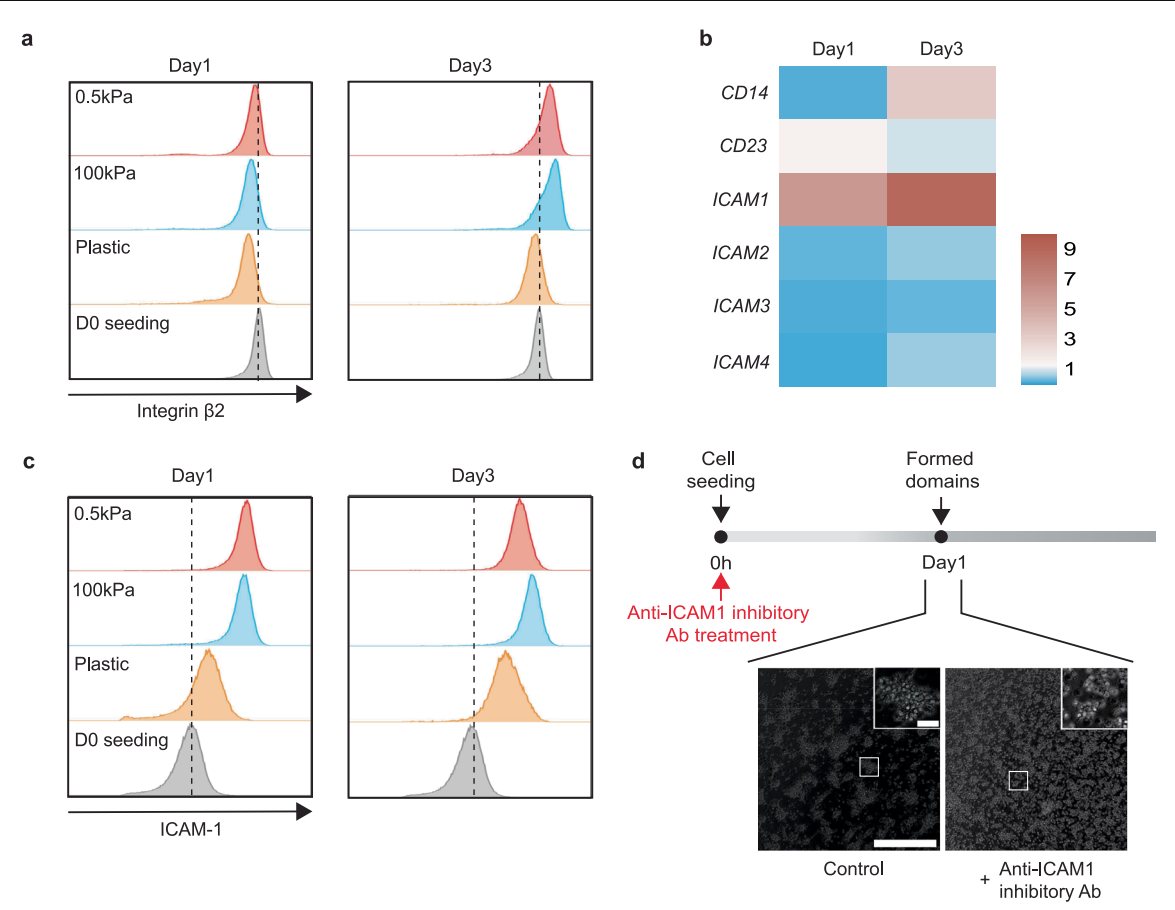
activated B cell/NK cell/T cell domain formation on day 1 and day 3. B cell and NK cell domains formed on day 1. These domains subsequently merged, leading to macroscopic phase separation on day 3. T cells formed a few small clusters with the majority of the cells remaining in the monolayer. Due to long-term activation and expansion, cellular viability dropped for these three common lymphocytes and dead cells could be visualized to be non-active during the observation window. Scale bar, $300\,\mu\text{m}$ (insets, scale bar, $30\,\mu\text{m}$).



Extended Data Fig. 2 | See next page for caption.

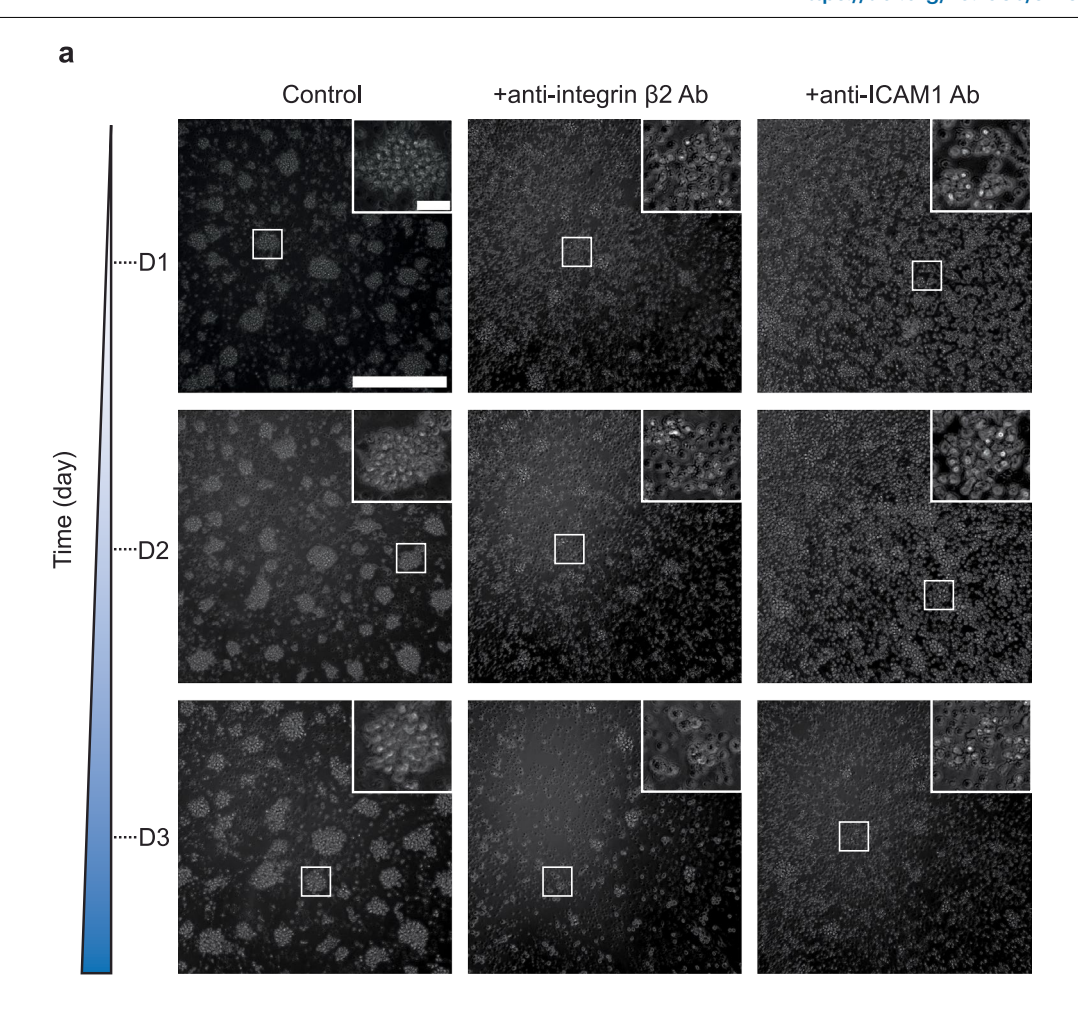
Extended Data Fig. 2 | **Effects of domain formation on monocyte viability and phagocytosis. a**, Domain formation and long-term maintenance of monocytes on collagen I-coated 0.5 kPa, plastic and glass substrates. **b**, Fold change in PrestoBlue (cell viability) signal normalized to day 0 when seeded. Notable cell death was observed for monocytes seeded on collagen I-coated plastic and glass substrates with dramatically decrease of PretoBlue signals compared to day 0. In the meantime, monocytes seeded on collagen I-coated 0.5 kPa substrate maintained a similar level of metabolic activity during the 3-day monitoring window, suggesting long-term maintenance with negligible effects from proliferation. **c**, Flow cytometry results of monocytes harvested from collagen I-coated 0.5 kPa, plastic and glass substrates on day 3. respectively. More cell debris and propidium iodide positive cells (died cells) were observed

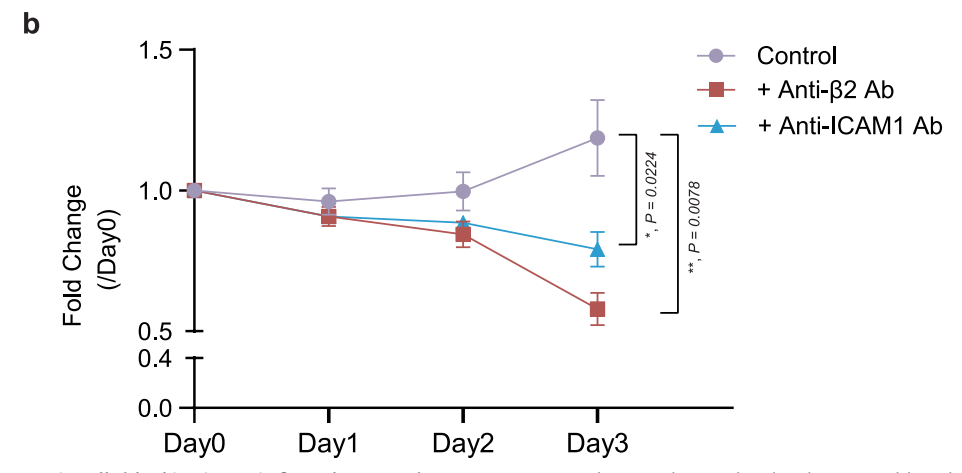
when monocytes were seeded on plastic and glass substrates. Representative immunofluorescence images of cells on different substrates were shown as merged images from phase and PI channel. **d**, Illustration that distinguishes monocytes inside and outside domains. **e**, Characterization of the phagocytic capabilities of monocytes inside and outside the domains, measured via quantification of GFP-positive carboxylate-modified polystyrene 1 µm beads intake after 6 h. Representative images in **a,c** were obtained with a phase-contrast microscope under 20x objective. Scale bars, 300 µm (insets, scale bar, 30 µm). Data in **b,e** are presented as mean \pm standard deviation; n = 3 independent biological samples for **e**; Two-tailed unpaired t test with Welch's correction was used for statistical analysis (**P \leq 0.01, *P \leq 0.05, ns P > 0.05) for **b,e**. Cartoon in **d** created with BioRender.com.



Extended Data Fig. 3 | ICAM-1 couples with $\beta 2$ integrin for intercellular adhesion to mediate domain formation. a, Flow cytometry offset histogram of integrin $\beta 2$ surface expression on day 1 (left) and day 3 (right) of monocytes seeded on collagen I-coated 0.5 kPa, 100 kPa and plastic substrates. Day 0 isolated monocytes were set as control. b, RT-qPCR analysis of the expression of putative integrin $\beta 2$ ligands using monocytes collected on day1 and day 3 from collagen I-coated 0.5 kPa substrate. Relative fold changes were measured relative

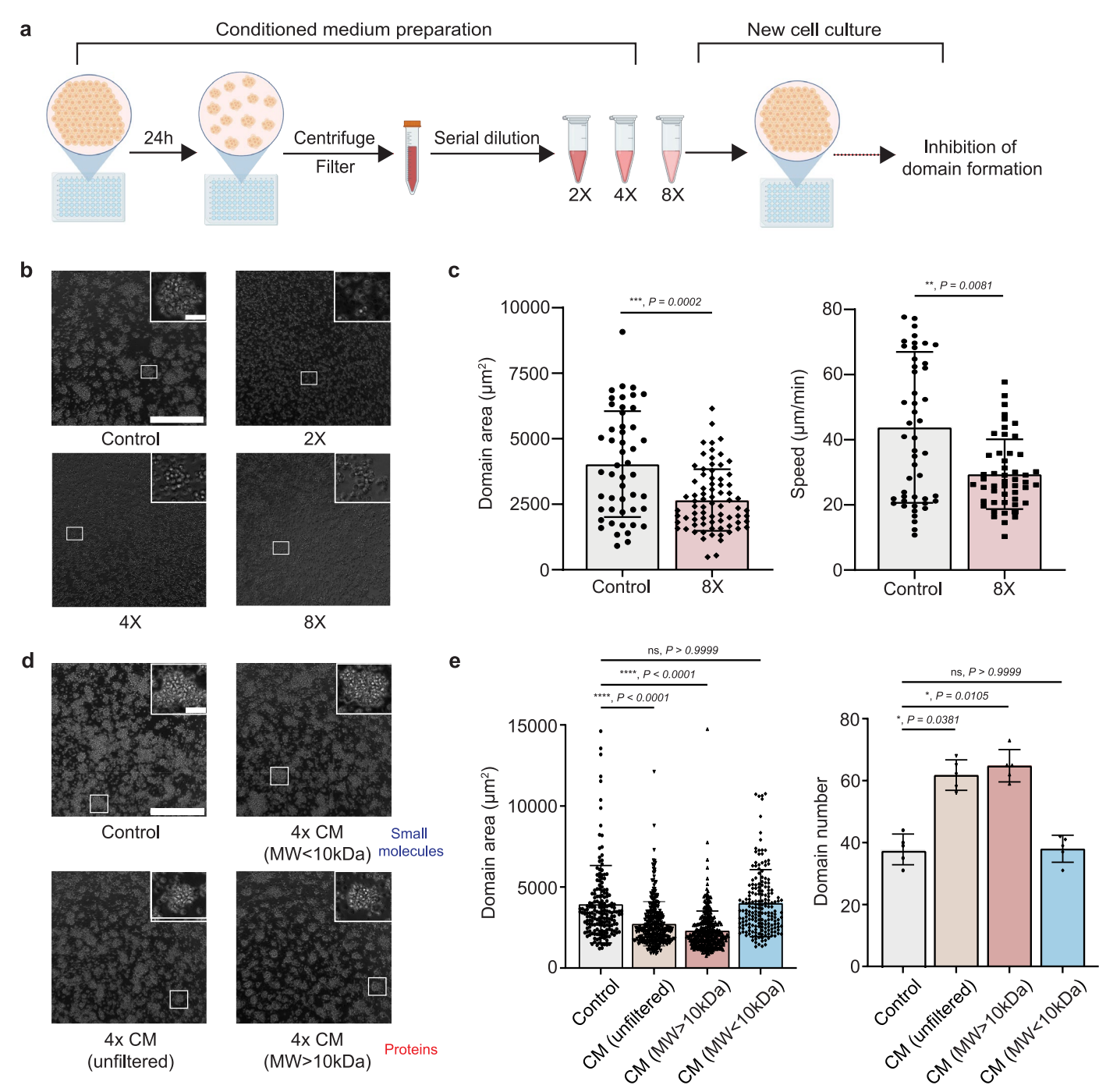
to day 0. *ICAMI* was found to be significantly upregulated on both day 1 and day 3. (n = 3 independent biological samples). **c**, Flow cytometry offset histogram of ICAM-1 surface expression on day 1 (left) and day 3 (right) for monocytes seeded on collagen I-coated 0.5 kPa, 100 kPa and plastic substrates. Day 0 isolated monocytes were set as control. **d**, Representative 20x phase-contrast images showing that monocytes treated with inhibitory ICAM1 antibody abrogated domain formation on day 1. Scale bars, 300 μ m (insets, scale bar, 30 μ m).





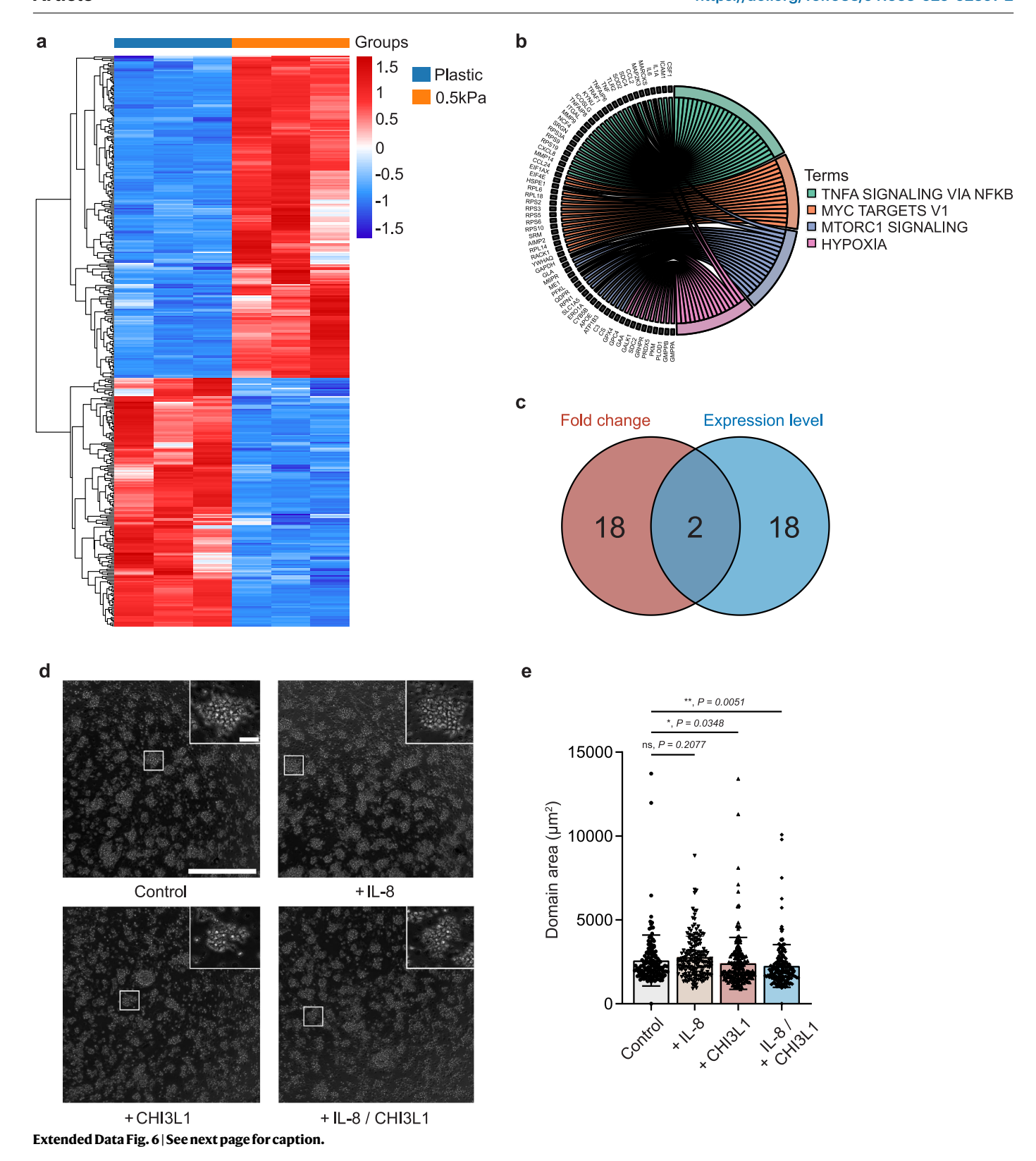
Extended Data Fig. 4 | Functionally blocking integrin $\beta 2$ and ICAM-1 abrogates monocyte domain formation. a, Representative 20x phase contrast images of monocytes seeded on collagen I-coated 0.5 kPa substrate treated with antiintegrin $\beta 2$ and anti-ICAM-1 antibodies obtained from day 1, day 2 and day 3. Under both conditions, domain formation was inhibited, and cell death was observed on day 3. Scale bars, $300 \, \mu m$ (insets, scale bar, $30 \, \mu m$). b, Fold change in

PrestoBlue signal normalized to day 0. Notably reduced viability was seen on day 3 when monocytes were treated with anti-integrin $\beta 2$ and anti-ICAM-1 antibodies. Data in \boldsymbol{b} are presented as mean \pm standard deviation with n = 3 independent biological samples. Two-tailed unpaired student's t-test with Welch's correction was used for statistical analysis (*P \leq 0.05, **P \leq 0.01).



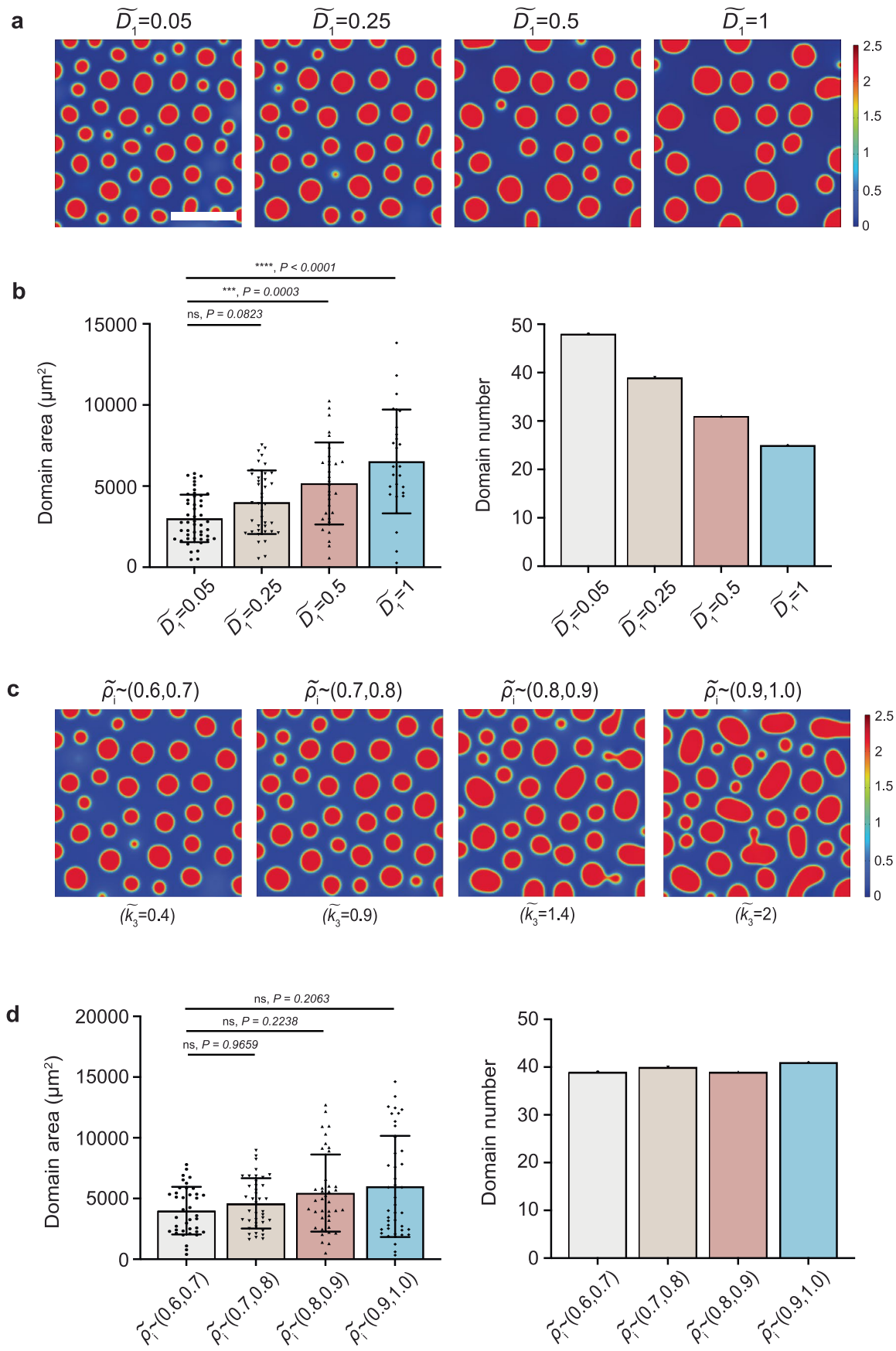
Extended Data Fig. 5 | **Conditioned medium from monocytic domains abrogates phase separation onset. a**, Illustration cartoon showing conditioned medium harvested from steady state monocyte domains negatively influenced the domains formation initiation in a concentration-dependent manner. **b**, Representative images of monocyte domains pre-treated with serial diluted conditioned media on day 1. 4x and 8x diluted conditioned media allowed for monocyte domains formation. **c**, Decreased steady state domains area and cell speed when monocytes were treated with 8x conditioned medium. **d**, Representative images of monocyte domains on day 1 pre-treated with control DMEM, complete conditioned medium (4x diluted), small molecules from conditioned medium (4x diluted) and proteins from conditioned medium (4x

diluted). **e**, Characterized domain areas and numbers of monocyte domains pretreated with different portions of conditioned medium on day 1. Representative images in **b**, **d** were obtained with a phase-contrast microscope under 20x objective. Scale bars, 300 μ m (insets, scale bar, 30 μ m). Data in **c**, **e** are presented as mean \pm standard deviation; n = 2 independent biological samples for **c**; n = 3 independent biological samples for **e**; all individual domains were measured from independent biological samples and plotted together in **c**, **e**. Two-tailed non-parametric Mann–Whitney test was used for statistical analysis (***P \leq 0.001) for **c**. Kruskal–Wallis test with Dunn's multiple comparisons test was used for statistical analysis (****P \leq 0.001, *P \leq 0.05, ns P'0.05) for **e**. Cartoon in **a** created with BioRender.com.



Extended Data Fig. 6 | **Identification of global inhibitors in the conditioned medium. a**, Conditioned media from monocytes seeded on plastic and 0.5 kPa substrates were harvested after 24 h and proceeded to proteomic assay (N = 3 independent biological samples, n = 3 technical repeats). A total of 32,554 peptides and 3,669 protein groups were identified for proteomic study, on average, the proteome had 3,611 protein groups per sample. The heatmap attached below revealed 402 proteins with significant differential expression (log2 fold-change >1; t test p < 0.05), in which 175 proteins downregulated and 227 upregulated in 0.5 kPa condition samples compared to plastic condition samples. **b**, Enrichment analysis on upregulated proteins. **c**, 2 candidate proteins were identified when intersecting the top 20 proteins with highest fold change and the top 20 proteins with the highest expression level. **d**, Representative 20x

phase contrast images of monocyte domains on day 1 with treatments of CHI3L1 (100 ng/mL), IL-8 (100 ng/mL) or combined (100 ng/mL each). Scale bars, 300 μ m (insets, scale bar, 30 μ m). \boldsymbol{e} , Domain area characterizations showed inhibition of domain formation when monocytes were treated with CHI3L1 instead of IL-8. Representative images in \boldsymbol{d} were obtained with a phase-contrast microscope under 20x objective. Scale bars, 300 μ m (insets, scale bar, 30 μ m). Data in \boldsymbol{e} are presented as mean \pm standard deviation with n = 3 independent biological samples; all individual domains were measured from independent biological samples and plotted together in \boldsymbol{e} . Kruskal–Wallis test with Dunn's multiple comparisons test was used for statistical analysis (**P \leq 0.01, *P \leq 0.05, ns P'0.05) for \boldsymbol{e} .



Extended Data Fig. 7 | See next page for caption.

Extended Data Fig. 7 | **Model predictions on motility and seeding density's effect on domain formation. a**, Simulation results illustrating steady state domain formation with monotonically decreased diffusion coefficient $\widetilde{D_1}$. All parameters except $\widetilde{D_1}$ were fixed. **b**, Characterization of domain area and domain number at different cell diffusion coefficient $\widetilde{D_1}$. Domain area increased with decreasing domain number. **c**, Simulation results illustrating steady state domain formation with monotonically increased initial cell density $\widetilde{\rho_i}$. Coefficient of interfacial energy $\widetilde{K_3}$ were changed correspondingly with different cell density $\widetilde{\rho_i}$ to reflect the energy density as a function of cell density. **d**, Characterization of

domain area and domain number at different initial cell density $\widetilde{\rho_i}$. All parameters except $\widetilde{\rho_i}$ and coefficient of interfacial energy $\widetilde{k_3}$ were fixed. All simulation results represent steady states at time $\widetilde{t}=20000$. All simulation results represent steady states. Scale bar, 300 μ m for all simulations. All domain area characterization results are presented as mean \pm standard deviation; all individual domains at steady state were measured from each simulation and plotted in \mathbf{b} , \mathbf{d} (n = 1 simulation). Kruskal–Wallis test with Dunn's multiple comparisons test was used for statistical analysis (****P \leq 0.0001, ***P \leq 0.001, ns P > 0.05) for \mathbf{b} , \mathbf{d} .

nature portfolio

| Corresponding author(s): | Denis Wirtz, Sean X. Sun |
|----------------------------|--------------------------|
| Last updated by author(s): | Jun 23, 2025 |

Reporting Summary

Nature Portfolio wishes to improve the reproducibility of the work that we publish. This form provides structure for consistency and transparency in reporting. For further information on Nature Portfolio policies, see our <u>Editorial Policies</u> and the <u>Editorial Policy Checklist</u>.

For all statistical analyses, confirm that the following items are present in the figure legend, table legend, main text, or Methods section.

| $\overline{}$ | | | | | |
|---------------|----|-----|-------|----|--------|
| Š | +~ | ١Ť١ | ist | т. | \sim |
| ٠, | - | | 1 N I | | |

| n/a | Confirmed |
|-------------|--|
| | The exact sample size (n) for each experimental group/condition, given as a discrete number and unit of measurement |
| | A statement on whether measurements were taken from distinct samples or whether the same sample was measured repeatedly |
| | The statistical test(s) used AND whether they are one- or two-sided Only common tests should be described solely by name; describe more complex techniques in the Methods section. |
| \boxtimes | A description of all covariates tested |
| | A description of any assumptions or corrections, such as tests of normality and adjustment for multiple comparisons |
| | A full description of the statistical parameters including central tendency (e.g. means) or other basic estimates (e.g. regression coefficient) AND variation (e.g. standard deviation) or associated estimates of uncertainty (e.g. confidence intervals) |
| | For null hypothesis testing, the test statistic (e.g. <i>F</i> , <i>t</i> , <i>r</i>) with confidence intervals, effect sizes, degrees of freedom and <i>P</i> value noted <i>Give P values as exact values whenever suitable.</i> |
| \boxtimes | For Bayesian analysis, information on the choice of priors and Markov chain Monte Carlo settings |
| \boxtimes | For hierarchical and complex designs, identification of the appropriate level for tests and full reporting of outcomes |
| \boxtimes | Estimates of effect sizes (e.g. Cohen's <i>d</i> , Pearson's <i>r</i>), indicating how they were calculated |

Our web collection on statistics for biologists contains articles on many of the points above.

Software and code

Policy information about availability of computer code

Data collection

- $1. \ All \ partial \ differential \ equations \ in \ the \ modeling \ part \ are \ solved \ using \ COMSOL \ Multiphysics \ 6.0.$
- 2. All the LC-MS/MS data were acquired via EvoSep coupled with timsTOF HT (Bruker, 4th generation) in data-independent acquisition mode.
- 3. All the RT-qPCR data were acquired via Bio-Rad CFX manager software (version 3.1).
- 4. All western blot images were acquired via Bio-Rad Image Lab software (version 6.0).
- 5. All flow cytometry data were acquired via FlowJo software (version 10.4).
- 6. All PrestoBlue cell viability data were acquired via Molecular Devices SoftMAX Pro software (version 7).

Data analysis

- 1. All partial differential equations in the modeling part are solved using COMSOL Multiphysics 6.0
- 2. All the MS/LS raw files were searched against a UniProt/Swiss-Prot database containing human proteins (downloaded on 02/07/2024, 20,433 entries) using the directDIA approach in the Spepctronaut (version 18, Biognosys).
- 3. All the RT-qPCR data were analyzed via Bio-Rad CFX manager software (version 3.1).
- $4. \ All \ western \ blot \ images \ were \ analyzed \ via \ Bio-Rad \ Image \ Lab \ software \ (version \ 6.0).$
- 5. All flow cytometry data were analyzed via FlowJo software (version 10.4).
- 6. All monocyte domain characterization (area / number / cell motility), qPCR data, PrestoBlue data were analyzed and plotted via GraphPad Prism (version 10.0.0).

For manuscripts utilizing custom algorithms or software that are central to the research but not yet described in published literature, software must be made available to editors and reviewers. We strongly encourage code deposition in a community repository (e.g. GitHub). See the Nature Portfolio guidelines for submitting code & software for further information.

Data

Policy information about availability of data

All manuscripts must include a data availability statement. This statement should provide the following information, where applicable:

- Accession codes, unique identifiers, or web links for publicly available datasets
- A description of any restrictions on data availability
- For clinical datasets or third party data, please ensure that the statement adheres to our policy

The proteomics raw data file that supports the findings of this study is publicly available online at https://www.ebi.ac.uk/pride/ under the accession PXD063197. Reviewers can access the dataset by logging in to the PRIDE website using the following account details:

Username: reviewer pxd063197@ebi.ac.uk

Password: ij5EqHJkrWOs

All the proteomics raw files were searched against a UniProt/Swiss-Prot database containing human proteins (downloaded on 02/07/2024, 20,433 entries) using the directDIA approach in the Spepctronaut (version 18, Biognosys).

Research involving human participants, their data, or biological material

Policy information about studies with <u>human participants or human data</u>. See also policy information about <u>sex, gender (identity/presentation)</u>, <u>and sexual orientation</u> and <u>race</u>, <u>ethnicity</u> and <u>racism</u>.

| Reporting on sex and gender | N/A |
|--|-----|
| Reporting on race, ethnicity, or other socially relevant groupings | N/A |
| Population characteristics | N/A |
| Recruitment | N/A |
| Ethics oversight | N/A |

Note that full information on the approval of the study protocol must also be provided in the manuscript.

Field-specific reporting

Please select the one below that is the best fit for your research. If you are not sure, read the appropriate sections before making your selection.

| ☐ Behavioural & social sciences | Ecological, evolutionary & environmental sciences |
|---------------------------------|---|
|---------------------------------|---|

For a reference copy of the document with all sections, see nature.com/documents/nr-reporting-summary-flat.pdf

Life sciences study design

All studies must disclose on these points even when the disclosure is negative.

Sample size

In this study, we in total included 3 human PBMC donors. The homotypic monocyte domain formation phenomenon of human primary monocytes and mechano-induced phase separation trends on different substrates introduced in Fig. 1/2 and Supplementary Fig. 1 was consistent among all 3 donors. The representative images were chosen from the first donor just for illustration, though. For RT-qPCR studies in Fig. 3, we included N=3 donors and n=3 wells for a total of 9 experiments per condition.

For measurements of the average domain size and number, we seeded monocytes isolated from different vials of PBMCs on 3 stiffness-gel plates from different batches as biological repeats. All identified domains were measured and characterized for all repeats and plotted in scatter plots (domains that got characterized were not the same number for different conditions but with all repeats combined together, we were able to characterize at least around 30-40 domains). Due to the limited number of monocytes we could isolate from one donor's blood sample, while investigating secreted inhibitory factors, cell motility and cell seed density's effect (Fig. 4/6/7), only one donor's monocytes were used.

Sample sizes were based on the availability of leukopaks from JHU School of Medicine and standard practices in the field for similar mechanobiology studies. We did not perform formal statistical methods . N=3 will always be underpowered but include 3 donors in a mechanobiology study is commonly viewed as robust.

Data exclusions

No data were excluded from analyses.

Replication

For experiments other than RT-qPCR, all key findings (including monocyte domain formation, phase separation on different substrates, and other imaging-based assays) were independently replicated at least three times. These replications involved either independent donor samples, different batches of substrates, or both. In all cases, the observed results were consistent across replicates, and all attempts at

| ren | lication | were | success | sful |
|-----|----------|------|---------|------|
| | | | | |

For RT-qPCR experiments, we performed three independent biological replicates using monocytes from three different donors (N=3), with triplicate wells per condition (n=3), yielding a total of 9 measurements per condition. We confirm that all RT-qPCR replicates were successful, and the expression trends were reproducible across all donors.

Randomization

Monocytes from different donors were allocated to experiments based on the order in which blood samples were received. When monocytes from one donor became limited, we transitioned to using monocytes from the next available donor. Allocation was not randomized due to the logistical constraint of primary cell availability. However, all experimental conditions were tested using cells from multiple donors, and key findings were consistent across donors, minimizing the impact of donor-to-donor variability. As such, covariates related to donor variability were inherently controlled by replication across different donors.

Blinding

We are blinded to group allocation for donor blood samples we received.

Reporting for specific materials, systems and methods

We require information from authors about some types of materials, experimental systems and methods used in many studies. Here, indicate whether each material, system or method listed is relevant to your study. If you are not sure if a list item applies to your research, read the appropriate section before selecting a response.

| Materials & experime | ntal systems | Methods |
|--|--|--|
| n/a Involved in the study | | n/a Involved in the study |
| Antibodies | | ChIP-seq |
| Eukaryotic cell lines | | Flow cytometry |
| Palaeontology and a | rchaeology | MRI-based neuroimaging |
| Animals and other o | rganisms | |
| Clinical data | | |
| Dual use research of | concern | |
| ⊠ Plants | | |
| | | |
| Antibodies | | |
| Antibodies used For antibody-based inhibitio | | n and activation of monocyte cell surface integrins: |
| | (2) Purified anti-human CD11 (3) Purified anti-human CD18 (4) Anti-hCD54 antibody: Bio (5) Anti-hCD49d antibody: Bi | B antibody: BioLegend, Cat# 302102, Clone# TS1/18. 1a/CD18 (LFA-1) antibody: BioLegend, Cat# 363402, Clone# m24. B antibody: Biolegend, Cat# 366302, Clone# CBR LFA-1/2. ellegend, Cat# 353102, Clone# HA58. ellegend, Cat# 304301, Clone# 9F10. evitrogen, Cat# MA1-80091, Clone# M1/70.15. |
| | For flow cytometry: | |
| | (3) PE anti-human CD54: Biol(4) APC Mouse IgG1, κ Isotyp | egend, Cat# 422301. olegend, Cat# 302113, Clone# TS1/18. legend, Cat# 353105, Clone# HA58. be Ctrl: Biolegend, Cat# 400121, Clone# MOPC-21. • Ctrl: Biolegend, Cat#400112, Clone# MOPC-21. |
| | For western blot: | |
| | (1) GAPDH (14C10) Rabbit m. (2) Integrin β2 (D4N5Z) Rabb (3) Anti-Rabbit IgG HRP-linke | " |

Validation

All antibodies were purchased directly from vendors and website links are attached below. Validation statements, relevant citations, and antibody profile in online databases can all be found on the manufacturer's website.

For antibody-based inhibition and activation of monocyte cell surface integrins:

(1) Purified anti-human CD18 antibody:

https://www.biolegend.com/en-us/products/purified-anti-human-cd18-antibody-851? Group ID=BLG4653 and Indiana. The products of the product o

(2) Purified anti-human CD11a/CD18 (LFA-1) antibody:

https://www.biolegend.com/nl-be/products/purified-anti-human-cd11a-cd18-lfa-1-antibody-10377? Group ID=BLG13333112. A substitution of the product of the p

(3) Purified anti-human CD18 antibody:

https://www.biolegend.com/de-de/products/purified-anti-human-cd18-antibody-10821?Clone=CBR%20LFA-1/2

(4) Anti-hCD54 antibody:

https://www.biolegend.com/de-de/products/purified-anti-human-cd54-antibody-7445?GroupID=BLG9560

(5) Anti-hCD49d antibody:

https://www.biolegend.com/en-ie/products/purified-anti-human-cd49d-antibody-586

(6) Anti-hCD11b antibody:

https://www.thermofisher.com/antibody/product/CD11b-Antibody-clone-M1-70-15-Monoclonal/MA1-80091

For flow cytometry:

(1) Human TruStain FcX:

https://www.biolegend.com/en-gb/products/human-trustain-fcx-fc-receptor-blocking-solution-6462?GroupID=BLG2181

(2) APC anti-human CD18:

https://www.biolegend.com/de-at/products/apc-anti-human-cd18-antibody-6575

(3) PE anti-human CD54:

https://www.biolegend.com/nl-nl/products/pe-anti-human-cd54-antibody-7447

(4) APC Mouse IgG1, κ Isotype Ctrl:

https://www.biolegend.com/fr-lu/products/apc-mouse-igg1-kappa-isotype-ctrl-fc-3034

(5) PE Mouse IgG1, κ Isotype Ctrl:

https://www.biolegend.com/de-de/products/pe-mouse-igg1-kappa-isotype-ctrl-1408

For western blot:

(1) GAPDH (14C10) Rabbit mAb:

 $https://www.cellsignal.com/products/primary-antibodies/gapdh-14c10-rabbit-mab/2118?srsltid=AfmBOorSa2E8Drq5oTahQB_-DaLyYOV2lTstgjhVoJEWnhiDrCTVNf78$

(2) Integrin β2 (D4N5Z) Rabbit mAb:

https://www.cellsignal.com/products/primary-antibodies/integrin-b2-d4n5z-rabbit-mab/73663?

srsltid = AfmBOoqFHxjXmAENqbaHuTNEZxFxRBeShGqX3T2WCyFiJKsPmJLIEDTD

(3) Anti-Rabbit IgG HRP-linked Antibody:

https://www.cellsignal.com/products/secondary-antibodies/anti-rabbit-igg-hrp-linked-antibody/7074?

srsltid=AfmBOopaxRer-6FB5_sY-wC-dkqQYJqF1_TIZPbWsAKuCj5oChdko-5i

In terms of choice-making for selected antibodies, we were referring to this paper:

Adam Byron, Jonathan D. Humphries, Janet A. Askari, Sue E. Craig, A. Paul Mould, Martin J. Humphries; Anti-integrin monoclonal antibodies. J Cell Sci 15 November 2009; 122 (22): 4009–4011. doi: https://doi.org/10.1242/jcs.056770

Flow Cytometry

Plots

Confirm that:

The axis labels state the marker and fluorochrome used (e.g. CD4-FITC).

The axis scales are clearly visible. Include numbers along axes only for bottom left plot of group (a 'group' is an analysis of identical markers).

All plots are contour plots with outliers or pseudocolor plots.

A numerical value for number of cells or percentage (with statistics) is provided.

Methodology

Sample preparation

Cell samples were washed 3 times in PBS and resuspended at a concentration of 1 million per mL. Cell suspensions were blocked with Human TruStain FcX (Biolegend) for 15 min under room temperature. The antibody staining solution was then added and incubated at 4 °C for 30 min. Antibodies used for cell labeling were as follows: APC anti-human CD18 (clone LFA-1/2, Biolegend), and Propidium Iodide solution (Biolegend) and concentration was set to 5uL per million cells. Wash cells and then resuspend cells in 350 μ L FAC wash buffer (1X DPBS containing 5% FBS, 1mM EDTA).

Instrument

BD FACS Canto

Software

FlowJo (version 10.4)

Cell population abundance

After preparation, cell samples were loaded to FACS Canto and the recording were set to 100,000 total events. single cell population is at 97.5% for 0.5kPa condition, 98.0% for plastic condition and 98.7% for glass condition.

Gating strategy

Live cell populations for different conditions were gated based on plotting FSC-A against SSC-A. Percentages of live cell populations were calculated by FlowJo using single cell population as parents. Histogram of PI channel were displayed for gated live cells.

Tick this box to confirm that a figure exemplifying the gating strategy is provided in the Supplementary Information.